Analysis of Mixing and Thrust Diagnostics for Shock Tunnel Hot Nozzle Testing

by

DOUGLAS ORIE CREVISTON

Bachelor of Science in Aeronautical Engineering
United States Air Force Academy, 1997

Submitted to the Department of Aeronautics and Astronautics
in partial fulfillment of the requirements for the degree of

MASTER OF SCIENCE IN AERONAUTICS AND ASTRONAUTICS

at the

MASSACHUSETTS INSTITUTE OF TECHNOLOGY

June 1999

Author: _____
Department of Aeronautics and Astronautics
May 7, 1999

Certified by: _____
Professor Ian A. Waitz
Associate Professor of Aeronautics and Astronautics
Thesis Supervisor

Accepted by: _____
Professor Jaime Peraire
Associate Professor of Aeronautics and Astronautics
Chairman, Departmental Graduate Committee

Abstract

Transient testing of hot engine exhaust nozzle flows is being pursued to enable cost and time savings of one to two orders of magnitude over steady-state hot-flow testing. This thesis presents the design and assessment of mixing and thrust measurement systems for use with a shock tunnel for these applications.

Results from preliminary testing of focused-Schlieren, shearing interferometer, and Mie-scattering systems are presented. The Mie-scattering method was judged to be most applicable to measure flow mixedness for this application. However, shortcomings in the tested Mie-scattering system were identified. An improved system is proposed which is expected to provide flow density measurements to within 5% uncertainty with an optical resolution on the order of 5-10 mm.

Starting with the typical design for a steady-state thrust measurement facility and an understanding of the differences between steady-state and shock tunnel testing, a thrust measurement system for use with shock tunnel testing was also developed. The requirement for a high frequency response demanded high structural stiffness in the thrust measurement system. Dynamic modeling confirmed the proposed thrust measurement system will satisfy that requirement. A detailed uncertainty analysis was used to identify the most important factors in the system uncertainty. The analysis suggests that the proposed thrust measurement system could be used to measure thrust coefficient to within 1% accuracy.

Acknowledgements

This thesis and the work behind it would not have been possible without the help of many people. First and foremost, I would like to thank Professor Ian Waitz for his guidance and assistance throughout my two years at MIT, and for the monthly team-building exercises that he held in high regard. Professor Peter Bryanston-Cross and Dr. Mark Burnett were highly involved in the effort to evaluate different possibilities for the mixing diagnostic system, and their involvement is much appreciated.

Dan Kirk and I spent many hours together in the small, windowless room that is the shock tunnel control room, and I value his friendship and professional expertise. Our complementary abilities and efforts have led to results we can both be proud of, and if I ever need someone to coat the surface of a room with fiberglass insulation in 95 °F, 95% humidity weather, I know who to call.

Thanks to Viktor Dubrowski and Jimmy Letendre for teaching me about machining and taking the time to slip a few of my jobs into their schedules, even if it meant giving up a break time.

The intramural basketball, football, and softball teams all have my fellowship, as one who went together with them through the surprisingly common thrill of victory and the occasional loss. Those were the days....

Cambridge Community Fellowship Church has been a wonderful group of friends and fellow workers during my stay in Cambridge. The great times with children and elderly of the community that have occurred because of CCFC have helped me keep life in perspective. Thanks especially to Karen for her patience and encouragement.

Finally, I thank my parents for teaching me how to live and supporting me as I've put those lessons into practice in environments far beyond what they imagined for me. Their words have stood every test.

This material is based upon work supported under a National Science Foundation Graduate Fellowship. Any opinions, findings, conclusions, or recommendations expressed by the author do not necessarily reflect the views of the National Science Foundation. Support for this work has also been provided by the Air Force Institute of Technology.

To the Glory of God

Table of Contents

ABSTRACT **3**

1 INTRODUCTION **7**

1.1 BACKGROUND 7

1.2 MIT SHOCK TUNNEL FACILITY 10

2 FACILITY OVERVIEW **11**

2.1 COMPARISON OF TRANSIENT AND STEADY-STATE FACILITIES 11

2.2 PRINCIPLES OF SHOCK TUNNEL OPERATION 13

2.3 RESEARCH HISTORY OF THE MIT SHOCK T UNNEL 16

3 MIXING MEASUREMENT SYSTEM **21**

3.1 HISTORICAL BACKGROUND 21

3.2 THEORETICAL BACKGROUND 23

3.3 OBJECTIVES OF AND REQUIREMENTS FOR THE MIXING MEASUREMENT SYSTEM 25

3.4 ATTEMPTED TECHNIQUES 25

3.5 PROPOSED MIXING MEASUREMENT SYSTEM 61

4 THRUST MEASUREMENT SYSTEM **66**

4.1 SYSTEM BACKGROUND 66

4.2 THEORETICAL BACKGROUND 67

4.3 HISTORICAL BACKGROUND 69

4.4 PROPOSED SYSTEM 71

5 CONCLUSIONS **80**

5.1 MIXING DIAGNOSTIC 80

5.2 THRUST DIAGNOSTIC 80

5.3 FUTURE WORK 80

6 APPENDIX A: DETAIL OF COPPER-VAPOUR LASER ATTEMPT AT MIE-SCATTERING MIXING MEASUREMENTS **83**

APPENDIX B: DETAILED THRUST MEASUREMENT SYSTEM UNCERTAINTY ANALYSIS **85**

List of Figures

Figure 1: Mixer-Ejector, Detail of Mixing Lobes 9

Figure 2: Shock Tunnel Wave History 13

Figure 3: Shock tunnel Primary Diaphragm Layout 16

Figure 4: Pressure Repeatability Demonstration 20

Figure 5: Focused-Schlieren Schematic 26

Figure 6: 1/4 inch conic nozzle, 10 millisecond exposure during steady-state testing 29

Figure 7: 1/4 inch nozzle, 1 millisecond exposure during transient testing 31

Figure 8: Interference of Two Beams 35

Figure 9: Shearing Interferometer Schematic 35

Figure 10: Mie-Scattering System Schematic 37

Figure 11: Plug Displacement 39

Figure 12: 1/4 inch nozzle, 5 millisecond exposure during steady-state testing 43

Figure 13: 1/4 inch nozzle, 30 microsecond exposure during steady-state testing 45

Figure 14: 1/4 inch nozzle, 5 millisecond exposure during transient testing 47

Figure 15: 1/4 inch nozzle, 30 microsecond exposure during transient testing 49

Figure 16: 4 inch nozzle, 0-1 diameters downstream, 5 millisecond exposure 53

Figure 17: 4 inch nozzle, 0-1 diameters downstream, 30 microsecond exposure 55

Figure 18: 4 inch nozzle, 1-3 diameters downstream, 5 millisecond exposure 57

Figure 19: 4 inch nozzle, 1-3 diameters downstream, 30 microsecond exposure 59

Figure 20: Off-Axis Nozzle Thrust Balance 68

Figure 21: Shock tunnel Nozzle Force Balance 68

Figure 22: Thrust System Schematic 70

Figure 23: Dynamic Model of Balance 73

Figure 24: Dynamic Response of Proposed System 76

1 Introduction

1.1 Background

1.1.1 Economic Demand for High Speed Civil Transport

Commercial air travel has become a permanent fixture of the global economic landscape. The air transportation market is expected to experience significant growth, especially in the trans-Pacific area. In Boeing's 1996 Current Market Outlook, air traffic was predicted to increase 5.1% per year worldwide and 7.1% per year in Asia throughout the period from 1996 to 2015.[1] The expected increase in air travel in this area has made the concept of a 300-passenger class supersonic air transport an attractive one to the United States aerospace industry. Currently, NASA and American aerospace industry leaders are participating in a joint research initiative to explore technologies necessary for such an aircraft, which has been designated the High Speed Civil Transport (HSCT). The HSCT program deals with a conceptual aircraft design that would transport approximately 300 passengers over 5,000 nautical miles at a speed of Mach 2.4.[2]

1.1.2 Motivation for Mixer-Ejector Research

One major impediment to any future implementation of a supersonic airliner is the predicted environmental impact. In a 1995 study, engine noise was identified as the most critical environmental impact issue for major airlines.[3] The only supersonic transport currently in operation is the Concorde, which exceeds the FAR 36 Stage III noise regulations by 12, 18, and 13 EPNdB

---

[1] Boeing Commercial Group Marketing. 1996 Current Market Outlook. March 1996. p. 1

[2] High Speed Research Overview Web page, http://www.lerc.nasa.gov/WWW/HSR/HSROver.html

[3] International Air Transport Association. Environmental Review 1996. P. 97

for sideline, cutback, and approach respectively.[4] For a future supersonic airliner to be commercially viable, it must be able to satisfy the relevant FAR noise regulations, enabling it to operate out of current airports without a special exemption. The HSCT program is currently researching methods for minimizing the noise associated with takeoff and approach/landing, so as to meet FAR regulations. The MIT shock tunnel facility exists to aid this research effort through evaluation of noise-suppressing nozzle designs. The objective of this thesis is to evaluate the feasibility and outline the implementation of thrust and mixing measurements that are needed for such an evaluation.

At takeoff and landing, the primary noise source is the mixing noise due to the exhaust jet. This noise is proportional to the eighth power of jet velocity, and significant noise reduction can only be expected if the jet velocity is significantly lowered. The current generation of subsonic transports accomplishes this through high bypass-ratios and the mixing of core and bypass flow, but this option is not open to the HSCT, which must be relatively low-bypass for supersonic cruise efficiency. A similar concept, however, is used by mixer-ejector nozzles which entrain outside flow and use lobed mixers to enhance mixing between the core and entrained flow, as shown in Figure 1.

---

[4] Smith, M.J.T., Lowrie, B.W., Brooks, J.R. and Bushell, K.W.: Future Supersonic Transport Noise - Lessons from the Past. AIAA Paper No. 88-2989.

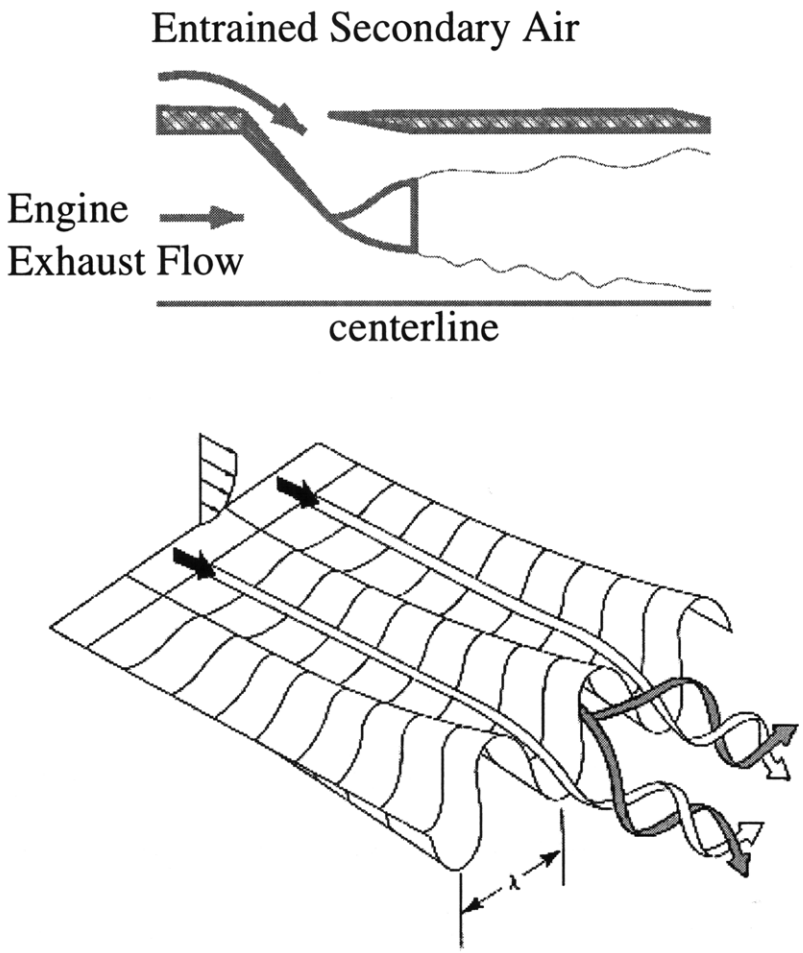

Figure 1: Mixer-Ejector, Detail of Mixing Lobes

A major difference between the turbofan and nozzle solutions, however, is that the high bypass-ratio design contributes to the overall efficiency of the engine, while a mixer-ejector nozzle exists solely for the purpose of noise reduction. Therefore, the mixer ejector must be designed to provide the necessary reduction in jet velocity within the shortest and lightest possible duct structure, while

not incurring prohibitive losses in engine thrust. The predicted noise reduction required varies from 20 decibels for a turbojet cycle engine to 1-2 decibels for a high-flow cycle engine.[5]

1.2 MIT Shock tunnel Facility

1.2.1 Facility Objectives

An understanding of the mechanics of flow mixing and noise generation within a mixer-ejector is essential to the design process of such a device, and can be obtained most effectively with the aid of a careful and exhaustive experimental study. A shock tunnel facility lends itself to such an experimental study for a wide variety of reasons. A shock tunnel is a mechanically simple device that uses a shock wave to uniformly heat and pressurize a test gas. Through careful control of the shock wave properties, nozzle pressure ratios (NPRs) from 1.5 to 4.0 and total temperature ratios (TTRs) from 1.5 to 3.0, the ranges of interest to the HSCT program, can be readily and consistently obtained. Given appropriate instrumentation, a shock tunnel can be used to measure the acoustic noise reduction and associated thrust loss for any HSCT mixer-ejector design. Furthermore, the addition of a flow visualization system may allow the identification of specific mixing structures and their correlation to the acoustic noise produced, increasing the effectiveness of the shock tunnel as a design tool. The shock tunnel has great potential as a rapid turn-around design tool for mixer-ejector nozzles because of its operating characteristics and low cost.

---

[5] Low Noise Exhaust Nozzle page, http://www.lerc.nasa.gov/WWW/HSR/CPCNozz.html, High Speed Systems Office.

2 Facility Overview

2.1 Comparison of Transient and Steady-State Facilities

2.1.1 Cost and Time-to-Test Comparison

Currently, the most common facilities for testing of jet engine exhaust nozzles are combustion or electric-arc heated, continuous flow tunnels. These facilities are able to obtain steady-state data on nozzle performance, but suffer from some characteristics that curtail their effectiveness as design tools. Steady-state facilities are large, extremely complex, and expensive to build and operate. An example is the Boeing Low Speed Aeroacoustic Facility (LSAF). The LSAF is capable of delivering mass flows up to 30 lb/sec and incorporates a propane burner to create temperatures of up to 1500 F.[6] Because the LSAF so effectively simulates the engine operating environment, the model nozzles it uses require high-strength, high-temperature materials which lead to more lengthy and expensive fabrication. The cost of a design study in such a steady-state facility is on the order of $100K-$1M dollars with a time-to-test on the order of 9 months, due to the increased difficulty in the design and fabrication of the mixer-ejector chute racks. In contrast, the cost and time-to-test to fabricate and test the same nozzle design using a shock tunnel is on the order of $10-100K dollars and 1-3 months, respectively.

---

[6] Boeing BTS - Acoustics - High Temperature Jet Simulator Page.
http://www.boeing.com/assocproducts/techsvcs/boeingtech/bts_acoub1.html

2.1.2 Test Article Comparison

The shock tunnel provides cost and time savings through its unique requirements for the test articles. Because steady-state facilities subject their test articles to pressure and temperatures typical of predicted HSCT operating conditions for long periods of time, the mixer-ejector designs must be fabricated from materials similar to what would actually be used in the HSCT. The shock tunnel, in contrast, achieves the pressures and temperatures of interest for only about 50 ms. Due to the transient nature of the test, the test article does not experience significant heating and hence may be fabricated of a much lower-cost material, such as plastic or cast aluminum. Furthermore, the test articles will experience no structural expansion due to heating, which implies that throat area and other geometric design parameters will be known to a higher degree of accuracy. The impact of this advantage is realized by the fact that steady-state chute racks have a cost on the order of $50K dollars, while shock tunnel chute racks have a cost on the order of $5K dollars, an order of magnitude less.

2.1.3 Shock tunnel Application to HSCT Program

The MIT shock tunnel exhausts into an acoustically-treated chamber and has already been used to make acoustic measurements of axisymmetric nozzles.[7, 8] A Large-Scale Model Similitude (LSMS) mixer-ejector model has also been fabricated for testing. The feasibility of thrust and mixing measurements is discussed in this thesis. While successful measurement of mixing noise, thrust coefficient, and flow mixedness is

---

[7] Kirk, D.R., D.O. Creviston, I.A. Waitz. Assessment of a Transient Testing Technique for Jet Noise Research. AIAA Paper 99-1866.
[8] Dan's thesis

expected, any one alone could make the shock tunnel a viable and valuable part of the HSCT mixer-ejector design process.

2.2 Principles of Shock Tunnel Operation

The fundamental purpose of a shock tunnel is to generate a reservoir of high temperature and pressure fluid that is expanded through a nozzle to create a hot supersonic jet. Initially, the tunnel is separated into a driven section, denoted as region (1), and driver section, denoted as region (4), by two thin diaphragms. The pressure wave history in the shock tunnel is shown in Figure 2.

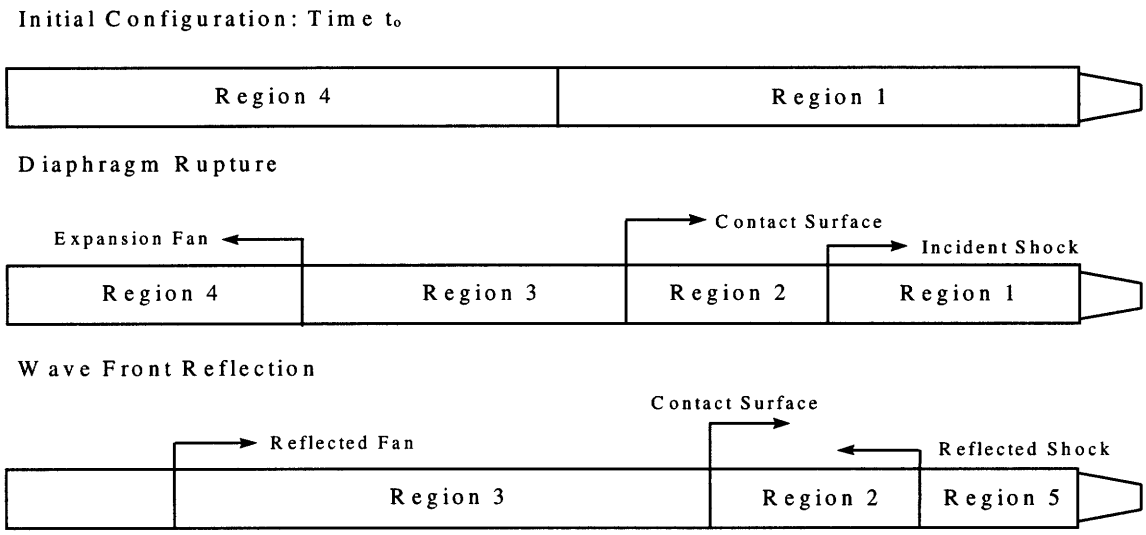

Figure 2: Shock Tunnel Wave History

The driven section contains the test gas, air for each test, and is typically evacuated to around $1/5^{th}$ of an atmosphere. The driver section is evacuated and then filled with a mixture of helium and air to a pressure between 2 and 6 atm depending on the desired shock strength. The shock tunnel affords a great deal of flexibility because both the driver pressure and gas composition as well as the test gas pressure can be easily and accurately regulated to yield different stagnation temperatures and pressures behind the reflected

shock. When the section of the tunnel between the two diaphragms is evacuated, the pressure difference causes the diaphragms to rupture. The driver gas acts like an impulsively started piston initiating a series of converging compression waves, rapidly compressing the test gas. The compression fronts coalesce into a shock wave, propagating through the driven section, accelerating and heating the driven gas. Concurrently, a series of diverging expansion waves propagate through the driver gas mixture decreasing the pressure and accelerating the fluid in the direction of the nozzle. The state of the gas which is traversed by the incident shock wave is denoted by region (2) in Figure 1, and that of the gas traversed by the expansion fan is denoted as region (3). The interface, or contact surface, between regions (2) and (3) marks the boundary between the gases which were initially separated by the diaphragm. Neglecting diffusion and Richtmyer-Meshkov instabilities, they do not mix, but are perpetually separated by the contact surface, which is analogous to the face of the piston. The test is initiated when the incident shock wave reaches the nozzle-end of the tunnel, reflects from the nozzle-end-plate, and creates a region of stagnant, high-pressure, high-enthalpy air, denoted as region (5) in Fig. 1c. This air can be expanded through a nozzle to the desired conditions.

On either side of the contact surface it is essential that the speeds of sound between regions (2) and (3) are identical to prevent extraneous waves from the reflected shock as it passes through the contact surface. These waves may substantially limit the available test time. To ensure that this does not occur, the speed of sound is matched by choosing the appropriate composition of gases for the driver section, using the matching condition:

$$\frac{\gamma_2}{a_2^2}\left[(\gamma_2+1)\frac{p_5}{p_2}+\gamma_2-1\right]=\frac{\gamma_3}{a_3^2}\left[(\gamma_3+1)\frac{p_5}{p_2}+\gamma_3-1\right] \qquad \text{Eq. 2.1}$$

The shock strength can be determined using the basic shock tunnel equation which relates the shock strength, p_2/p_1, implicitly as a function of the known diaphragm pressure ratio p_4/p_1:

$$\frac{p_4}{p_1}=\frac{p_2}{p_1}\left[1-\frac{(\gamma_4-1)(a_1/a_4)(p_2/p_1-1)}{\sqrt{2\gamma_1}\sqrt{2\gamma_1+(\gamma_1+1)(p_2/p_1-1)}}\right]^{\frac{-2\gamma_4}{\gamma_4-1}} \qquad \text{Eq. 2.2}$$

Once the shock strength is determined, all other flow quantities can be calculated from normal shock relations, and thus the thermodynamic and fluid mechanic properties of the jet are predicted.

2.3 Research History of the MIT Shock T unnel

2.3.1 Diaphragm Bursting

Obtaining useful data from the MIT shock tunnel involves two basic operations: firing the shock tunnel to produce the correct flow conditions and recording the resulting physical phenomena. An essential component of firing the shock tunnel correctly is the ability to control the pressures in the driver and driven sections and the helium/air mass fraction in the driver section at the time of firing. This is accomplished through three control transducers coupled through a National Instruments LabView Virtual Instrument to control two MKS mass flow controllers. The Virtual Instrument has been designed to automate the evacuation of the driven section and the pressurization of the driver section.

Insuring rapid but predictable diaphragm rupture is the other essential element for a successful shock tunnel test. The diaphragms used in the MIT shock tunnel are composed of untempered Aluminum 3003 alloy sheet metal. The shock tunnel is operated so that two diaphragms equally share the pressure load while the driver and driven sections are being brought to their appropriate pre-test conditions, as shown in Figure 3.

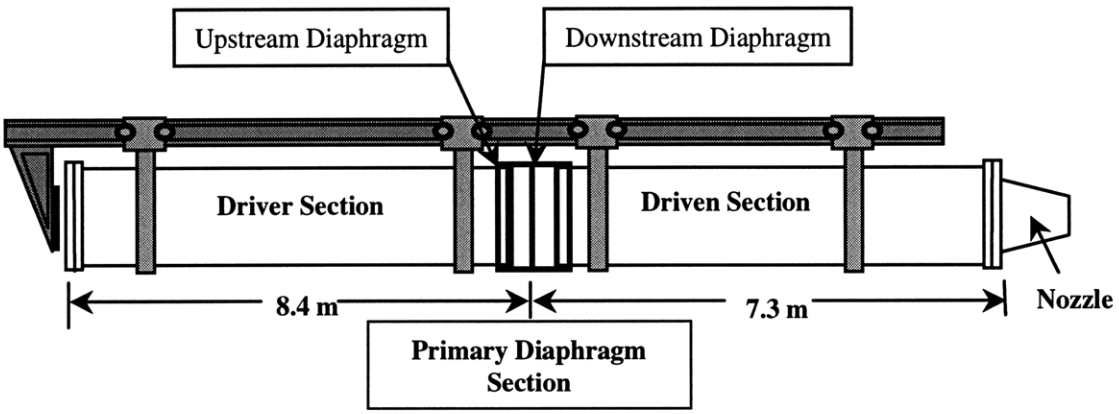

Figure 3: Shock tunnel Primary Diaphragm Layout

When the test is to be initiated, the entire pressure load is placed first upon the upstream diaphragm by evacuating the space between the diaphragms. Then, after the first diaphragm ruptures, the downstream diaphragm sees the full pressure load and ruptures. Initially, this was accomplished through the use of knife blades arrayed in a cruciform pattern. These were positioned just aft of the diaphragms, and cut the diaphragms as they deflected under the pressure load. Some difficulties were experienced using the knife-blades, however. First, the distance between the knife blades and the undeflected diaphragm was found to be crucial. Since the amount of deflection was unknown, this position was found through trial and error for each set pressure. The set pressure varies with the desired nozzle flow parameters, so finding the correct knife blade position was a laborious process. Second, the knife blades were sometimes found to actually support the diaphragms during their deflection rather than piercing them. This is reasonable when one considers how much force would be necessary to drive an edge through sheet metal at a right angle. Third, slivers of sheet aluminum were being sliced off by the knife blades as the diaphragm petals oscillated during the shock and expansion fan reflections. These aluminum slivers could damage the flowpath surfaces over time.

The current system for diaphragm rupturing has shown itself to be much more effective. One material is used for the diaphragms, Aluminum 3003 alloy, but this material is used in three thicknesses – 0.012", 0.016", and 0.020". Burst tests have been performed to identify the bursting pressures for these three materials. Scoring in a cruciform pattern on the diaphragm causes a uniform breaking pattern, just as the knife blades did. Furthermore, selecting the correct thickness diaphragm based upon the burst

pressure and desired set pressure leads to reliable rupturing. The thickness chosen, after the appropriate scoring, must be able to bear half the pressure difference that exists between the driver and driven sections to allow test preparation, while failing under the full pressure difference between driver and driven sections to allow test execution. There are no aluminum slivers created using this method if done correctly.

2.3.2 Instrumentation and Data Acquisition

Accurately measuring and recording the physical phenomena produced is accomplished through the shock tunnel instrumentation. Four Kulite XT-190 pressure transducers operate with a resonance frequency of 160 kHz, enabling them to resolve pressure changes experienced in the facility. Six Bruel & Kjaer 4135 free-field microphones are also installed to record acoustic data. The transducer outputs are recorded using Adtek AD830 data acquisition boards taking data at 200 kHz. Currently, four AD830 boards are installed giving a total of 32 channels (20 channels available for expansion) which may be acquired simultaneously at up to 200 kHz. The pressure transducers are checked against a Paroscientific Model 740 laboratory standard before every test and are calibrated as needed. The data acquisition system has been checked using a function generator and has been shown to have insignificant signal attenuation for frequencies up to 100 kHz. Background noise measurements have confirmed a high signal to noise ratio. The background noise is on the order of 10 dB lower than the measured signal. The instrumentation system is capable and proven.

2.3.3 Experimental Results

As a new facility, the MIT shock tunnel has been proved to perform in the expected manner and to provide the necessary flow characteristics before any experimental apparatus can have a hope of success. Through several hundred tests, the MIT Shock tunnel has been shown to function according to the shock tunnel theory, and has proven itself to be capable of supporting experimental testing. Nozzle flows of interest may be precisely defined by two quantities, Nozzle Pressure Ratio (NPR) and Total Temperature Ratio (TTR). The shock tunnel has established its ability to consistently and accurately produce flows with well-defined NPR and TTR. Figure 4 shows the pressure traces for the same pressure transducer from six *different* shock tunnel tests. The pressure traces are virtually identical, with small oscillations about the mean providing the only discernible difference. The useful test time is approximately 12 ms, as expected. This plot also shows the possibility for improvement in test time length, which is being investigated, but is not pertinent to this discussion.

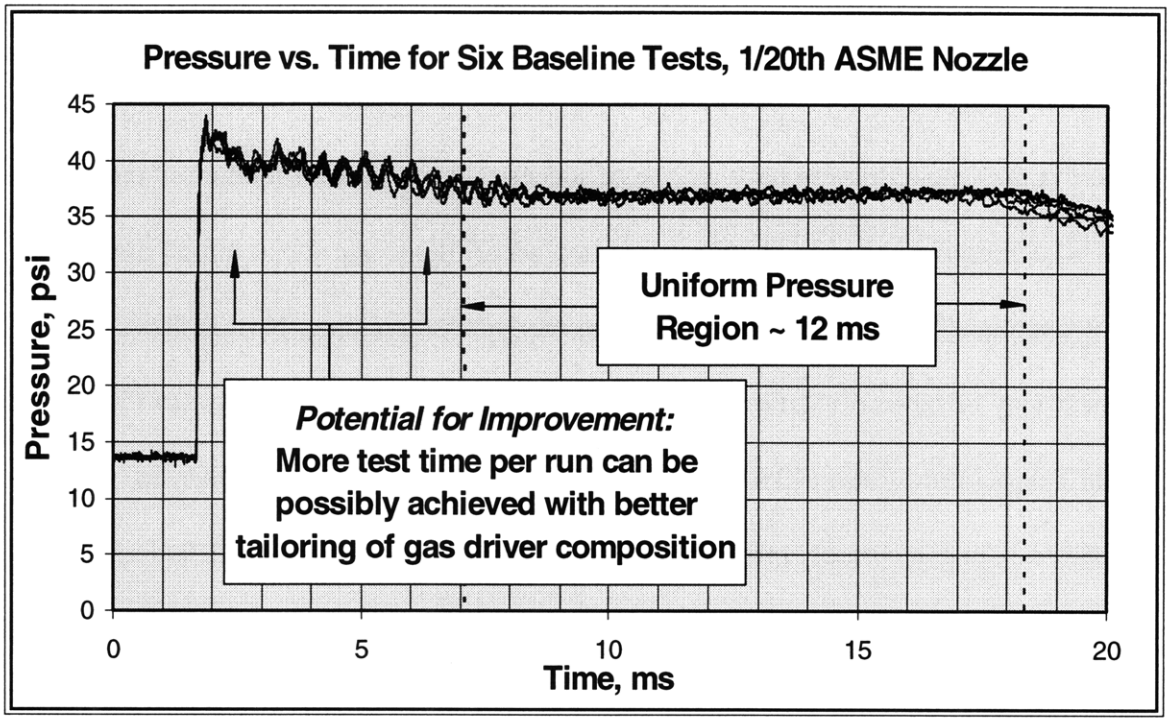

Figure 4: Pressure Repeatability Demonstration

TTR is calculated from measured incident shock speed, and has demonstrated repeatability to within 1%. The MIT shock tunnel has demonstrated the capability to accurately and reliable produce nozzle flows needed for thrust and mixing testing within the HSCT program.

Acoustic results have been obtained which indicate that the jet is fully developed and exhibits quasi-steady behavior suitable for testing. Acoustic measurements show that the transient noise data agrees with the steady-state data to within +/- 2-3 dB. Depending on the Nozzle Pressure Ratio and Total Temperature Ratio, transient and steady-state EPNL are shown to agree within 1-3 dB.[9]

---

[9] Kirk, D.R., D.O. Creviston, I.A. Waitz. Assessment of a Transient Testing Technique for Jet Noise Research. AIAA Paper 99-1866.

3 Mixing Measurement System

3.1 Historical Background

The goal of the MIT shock tunnel optical diagnostic system is to provide a measure of the flow mixedness at various downstream stations and an understanding of how that mixing is accomplished. Related measurements have been made in the past by numerous other research initiatives. A shadowgraph and Schlieren system was used by Opalka to obtain images of convergent-divergent nozzles within a shock tunnel.[10] This system was able to capture images of the starting flow associated with a nozzle mounted downstream of a shock tunnel diaphragm, to include starting and quasi-steady shocks. No mixing measurements were made in that effort. While this demonstrates the feasibility of optical diagnostics in the shock tunnel environment, the specific objectives of the MIT shock tunnel require a method with the capability to make mixing measurements, which the Schlieren and focused Schlieren systems can not provide.

Another possible optical diagnostic for the shock tunnel, the interferogram, has been shown to produce quantitative density field measurements. Nakamura and Iwamoto have used Mach-Zehnder interferograms to quantify the density distribution within an axisymmetric flowfield for a free jet and a jet impinging upon a plate for nozzle pressure ratios from 2.0 to 4.0.[11] The jet was unheated and was operated in a steady-state condition. Density measurements were made which exhibited good agreement with a numerical solution using a multi-grid TVD scheme. These encouraging results suggest that such a system could be implemented in the MIT

---

[10] Opalka, Klaus-Otto. Optical Studies of the Flow Start-Up in Convergent-Divergent Nozzles. AIAA Paper 95-12507.

[11] Nakamura, Tomoyuki, and Junjiro Iwamoto. A Quantitative Analysis of Axisymmetric Flow with Shock Waves from Interferogram. AIAA Paper 97-34025.

shock tunnel to make density field measurements for axisymmetric flows with similar flow properties.

Flow-tracer methods have also been used in applications similar to the MIT shock tunnel. A study done at the Princeton University Mach 8 wind tunnel demonstrated the ability to make instantaneous, planar images of high-speed, transient flows.[12] The Princeton Mach 8 wind tunnel is a blow-down type tunnel using air as the test gas. For the study in question, the tunnel was operated with a flow stagnation temperature of 494 K and a stagnation pressure of 3.8 MPa. Steady flow was achievable for one to two minutes at these conditions. A fuel injector design was used to inject helium (used in place of hydrogen) seeded with sodium particles into the hypersonic flow. The sodium particles were excited using a pulsed-dye laser at the 589 nm sodium D2 line. The laser operated with a repetition rate of 10 Hz, producing pulses of approximately 10 ns duration. The laser-induced fluorescence of the sodium was captured by an intensified CID camera. This study found that single pulse energies on the order of 100 microjoules were sufficient to make the planar laser-induced fluorescence images. Using this system, the Princeton team was able to capture images showing the mixing of the injected helium "fuel" with the free-stream flow. A similar optical diagnostic could be used in the MIT shock tunnel to make planar mixing measurements for axisymmetric nozzles or a 2-D mixer-ejector. While the flow duration in the MIT shock tunnel is one the order of 10 ms as opposed to a minute, the flow is quasi-steady in both cases. Different requirements would be placed upon the experimental equipment, but the conceptual basis of the Princeton study is transferable to the MIT shock tunnel application.

---

[12] Yalin, A.P., W.R. Lempert, M.R. Etz, P.J. Erbland, A.J. Smits, and R.B. Miles. Planar Imaging in a Mach 8 Flow Using Sodium Laser-Induced Fluorescence. AIAA Paper 96-2270.

A Mie-scattering imaging system has also been used by Tew to study mixing rates for lobed mixer-ejector nozzles.[13] Instantaneous and time-averaged mean images were obtained using liquid methanol seeding and a pulsed Nd:Yag laser for supersonic flows through square-lobed mixer-ejectors. The instantaneous images had a pulse duration of 10 ns while the time-averaged images were of 33 ms duration. Image processing was developed and utilized to successfully correct for background scattering, laser sheet intensity variations, and perspective distortions. Images were processed onto a passive scalar valued at 0 in no-seed regions and 1 at the maximum seed density, giving an understanding of the seed density throughout the image area. Although this study was done in a continuous-flow facility, the method is also directly applicable to the shock tunnel quasi-steady nozzle flow.

3.2 Theoretical background

3.2.1 Theory of Mie-scattering

The basic idea of flow tracer imaging methods is to seed the flow of interest with particles that will follow the motion of the flow, but be visible to the imaging apparatus. To accomplish this, the system must fulfill three conditions: the tracers must be small enough to follow the flow motion, the tracers must be sufficiently numerous to allow measurements throughout the flow, and the tracers must be visible to the imaging equipment. Past experience has shown that a particle diameter of less than 2 microns is necessary to faithfully follow the turbulence found in a 20 m/s flow.[14] In the more challenging case of a transonic shock, the

---

[13] Tew, D.E. Streamwise Vorticity Enhanced Compressible Mixing Downstream of Lobed Mixers. PhD. Thesis, MIT, 1997.
[14] Bachalo, W.D., R.C. Rudoff and M.J. Hauser. Laser Velocimetry in Turbulent Flow Fields: Particle Response. AIAA paper 87-0118, 1987.

particles must have a diameter on the order of 0.2 microns to faithfully follow the flow.[15] Seed density is controlled by the amount of seed added to the flow and is hence straightforward.

Mie-scattering occurs whenever light is incident on particles with a diameter similar to or greater than the wavelength of the incident light. In such a case, the incident light is scattered in all directions (though not with uniform intensity). All wavelengths are scattered in all directions through Mie scattering. The other major type of scattering is Rayleigh scattering, where light is incident on a particle with diameter smaller than the wavelength of the light. Some of the radiation is transmitted through this interaction. Unlike the omni-directional scattering of Mie scattering, reflected light in a Rayleigh interaction is scattered with dependency on the fourth power of the wavelength—therefore the shorter wavelengths are reflected much more than longer wavelengths.[16]

Some flow tracer techniques, such as Particle Imaging Velocimetry(PIV), require that each seed particle be visible to the imaging equipment. PIV uses the spatial position of each particle at two instants separated by a specified time interval on the order of a microsecond to determine the velocity of each particle. This is the most demanding of the flow tracer techniques, but also promises the greatest reward in the form of a complete velocity field. Such a technique imposes strict requirements for the amount of light that must be scattered by the particle, and hence the intensity required of the light source.

Assuming that the flow is uniformly seeded, the scattered light intensity per unit area may be measured as opposed to the individual particle reflections. Then the scattered light intensity may be used to infer information as to the seed density in the local region. This

---

[15] Thomas, P.J. A Numerical Study of the Influence of the Basset Force on the Statistics of LDV Velocity Data Sampled in a Flow Region with a Large Spatial Velocity Gradient. 1997, Exp. In Fluids, Vol. 23. Pp. 48-53.
[16] http://www.vislab.usyd.edu.au/photonics/fibres/fizzz/scattering2.html

technique utilizes an understanding of Mie-scattering, and is well-suited for mixing measurements.

Mie-scattering visualization may be improved if the measured intensity can be made independent of particle velocity. This is accomplished through shortening the exposure time of the imaging device so that seeding particles appear motionless, i.e. contained within one pixel of the image. This bears with it an associated increase in the required light intensity. Through such a method, however, the presence and qualitative characteristics (i.e. density) of the seeded flow may be determined, allowing useful mixing measurements.

3.3 Objectives of and requirements for the mixing measurement system

3.4 Attempted techniques

3.4.1 Focused-Schlieren System

In the course of evaluating the feasibility of mixing measurements using the MIT shock tunnel, three different imaging methods were attempted: a focused-Schlieren, a shearing interferometer, and a Mie-scattering imaging system. The Mie-scattering system was found to be most suitable for the mixing measurements to be made in the shock tunnel. The focused-Schlieren system was used to develop the triggering system necessary for the other diagnostics and to confirm the development of nozzle flow. The shearing interferometer was designed to give density field measurements for a low system cost and complexity, and was also used to diagnose the triggering system. All three imaging methods are discussed with the pertinent results from each.

The first is the focused-Schlieren system, which uses the deflection of light rays due to changes in index of refraction. A detailed description of the focused-Schlieren system and its relation to traditional Schlieren systems is given by Weinstein.[17,18] For the purposes of this thesis, a more general understanding will suffice. Light is projected through a large Fresnel lens, a source grid of equally spaced lines, and then through the flow field to be imaged. If changes of refractive index exist within that flow field, some of the light will be deflected from its original path. On the other side of the flow field, an imaging lens directs light from a specific plane within the flow onto a cut-off grid created from the source grid, which removes undeflected light, allowing only the deflected light to continue into the imaging plane. In practice, there is always some inaccuracy or misalignment between the source and cut-off grids, but this is a minor problem because the refracted light merely appears as relative lightening/darkening of the background illumination. A schematic of the focused-Schlieren setup is shown in Figure 5.

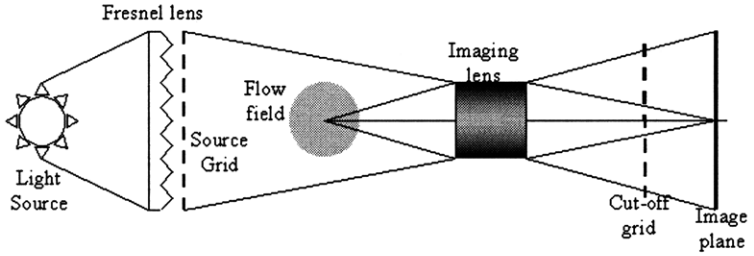

Figure 5: Focused-Schlieren Schematic

Due to the nature of the system, the focused-Schlieren method requires large changes in the refractive index to produce clear images. This effect is accentuated in the focused-Schlieren system because the image is drawn from deflections which occur within a plane of the flowfield, whereas the traditional Schlieren system creates an image from the bending experienced

---

[17] Weinstein, Leonard M. "Large Field High-Brightness Focusing Schlieren System." AIAA Paper 91-0567.
[18] Weinstein, Leonard M. "Designing and Using Focusing Schlieren Systems." NASA LaRC paper, Feb. 1992.

throughout the flowfield. Thus the change in refractive index must be large within a narrow plane rather than across an entire jet. Due to this fact, shock waves are the most readily distinguishable flow features using a focused-Schlieren system.

Tests were conducted using a focused-Schlieren system and the MIT shock tunnel facility. A ¼" diameter axisymmetric nozzle was used with images acquired during both steady-state and transient operation. Steady-state operation is achieved at the shock tunnel facility through the use of compressed air, while transient operation refers to the actual acquisition of data during the 12-15 ms test time of a shock tunnel run. The results are presented in Figures 6 and 7.

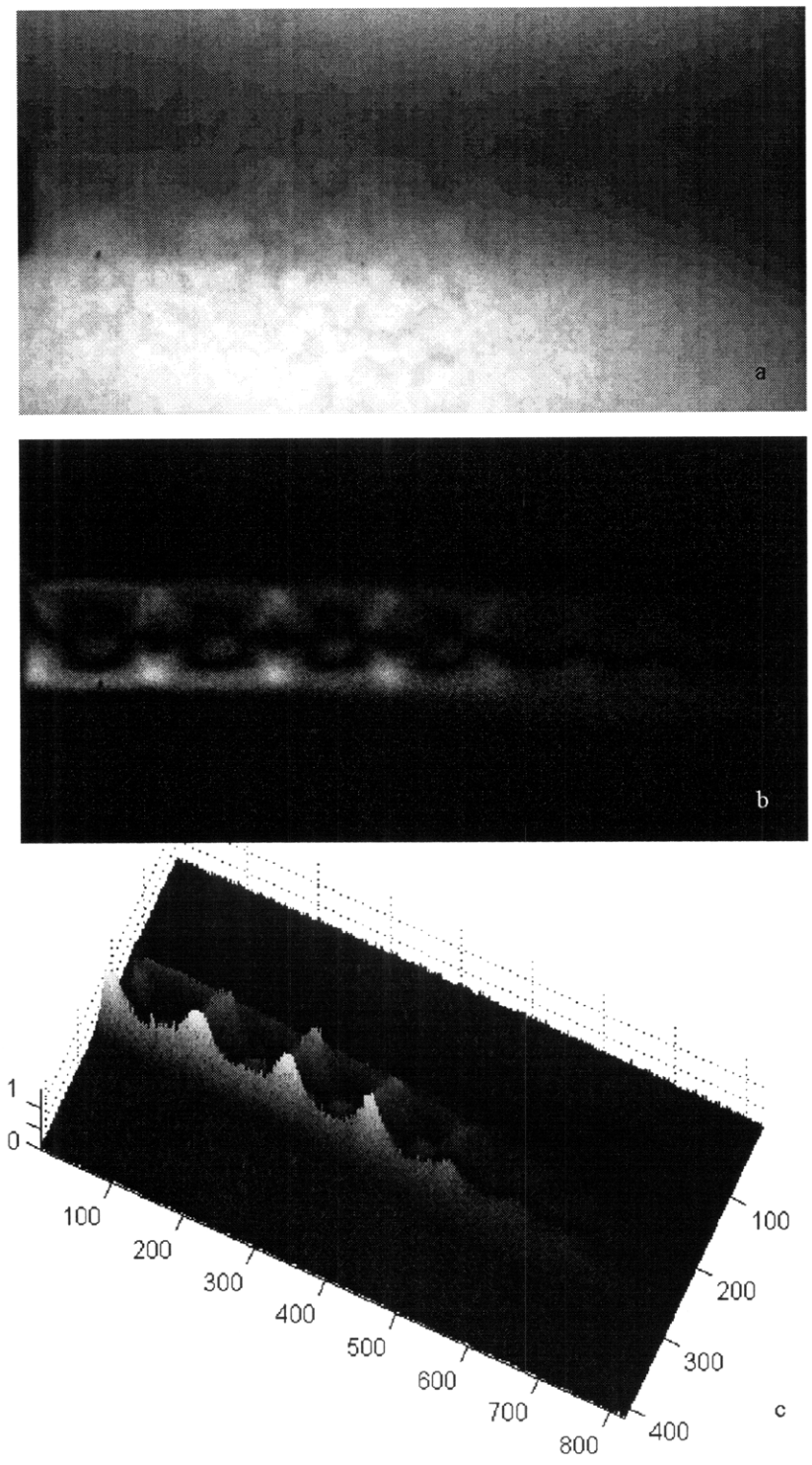

Figure 6: 1/4 inch conic nozzle, 10 millisecond exposure during steady-state testing

a) Raw Schlieren image
b) Schlieren image after background subtraction
c) Extended color depth over normalized surface

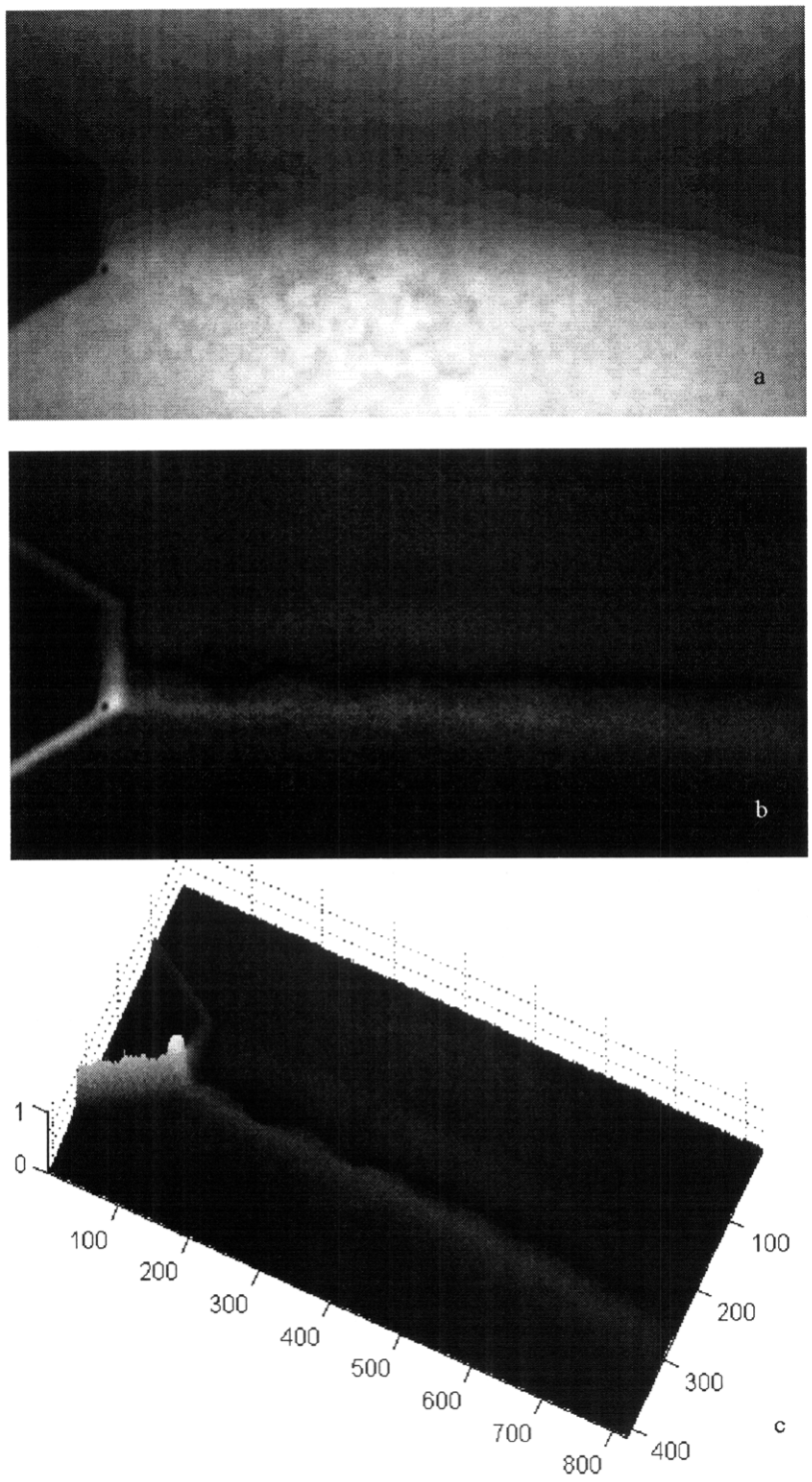

Figure 7: 1/4 inch nozzle, 1 millisecond exposure during transient testing

a) Raw Schlieren image
b) Schlieren image after background subtraction
c) Extended color depth over normalized intensity surface

The shock structure is visible during the steady-state tests, which gives an idea of the capabilities presented by the focused-Schlieren method. The transient image is less defined, though the shock structure is still there. This is partially due to the fact that there is a less pronounced difference between the refractive index of the transient jet and the surrounding atmosphere than in the steady-state case. The steady-state jet is at a NPR of approximately 3.0, but a TTR of 1.0 (no heating is applied to the compressed air). This gives a total density ratio of approximately 3.0 between the jet and the surrounding air. The transient case is tested at a NPR and TTR of approximately 2.5, a case representative of those targeted by the HSCT program. This leads to a total density ratio of approximately 1.0 between the jet and the atmosphere. This difference in the density gradient between the two flows makes it impossible to make use of the images as a comparison tool between the steady-state and transient methods of testing.

The focused-Schlieren method is judged to be unsuitable for the mixing measurement application at the MIT shock tunnel. Testing at NPR and TTR of interest to the HSCT program yields flows with total density approximately equal to that of the surrounding air, resulting in weak density gradients and hence images of poor resolution. Furthermore, since mixing is the desired quantity, it would be wiser to use a method that measures this directly as opposed to a shock-visualization method.

3.4.2 Shearing Interferometer

Shearography is a method using interferometry to identify the density field within a test region. The system relies upon differences in optical path length, and uses phase differences induced by changes in optical path length to identify changes in refractive index.

$$\mu - 1 = C\rho$$

μ= refractive index
ρ=density
C=Gladstone-Dale constant Eq. 3.1

For compressible flows (M>0.3), density throughout a flow field may be non-uniform as compressibility effects become important. These density non-uniformities change the way light propagates through the flow field through changes in the local refractive index. The Gladstone-Dale equation (3.1) quantifies the relationship between density and refractive index and illustrates it to be an approximately linear one.[19] Thus higher density leads to a higher refractive index.

Refractive index is related to the speed at which light propagates through the medium, so a higher refractive index will slow down light relative to a lower refractive index. Optical path length is a concept that quantifies this change in velocity as a change in length. A ray which travels through a region of higher density (and hence travels more slowly) is said to have a longer optical path length than a ray which travels through a region of lower density (and hence with a higher propagation velocity). Discounting the effects of refractive bending, the difference in optical path length(Ψ) is given by the following equation.[20]

$$\Delta\psi(x,y) = \int \mu(x_1 y_1 z_1) - \mu(x_2 y_2 z_2)dz = \int \Delta\mu(x,y,z)dz = N\lambda \qquad \text{Eq. 3.2}$$

These two equations may be combined, with an assumption of two-dimensionality making the dz term constant, to yield the following relation for change in density.

---

[19] Weinstein, Leonard M. "Designing and Using Focusing Schlieren Systems." NASA LaRC paper, Feb. 1992.
[20] Hecht, Eugene, and Alfred Zajac. Optics. Addison-Wesley Publishing Co. Reading, MA. 1974. P. 68.

For this to be practical, a method of determining the difference in optical path length must be available. Interferometry accomplishes this through the combination of two coherent beams to form an interference pattern. This interference pattern takes the form of light and dark fringes, which represent the phase difference, and therefore the optical path difference, between the two beams.

The shearing interferometer shown in Figure 9 is an effective means of accomplishing interferometry. The two beams needed to create the interference pattern both have their source in the same beam, but are separated by a back-silvered mirror. The glass surface of this mirror reflects part of the incident light, and the rest is reflected by the back-silvering creating two slightly-displaced beams. This system has the advantage of being relatively insensitive to rigid-body motion as opposed to a system with two truly independent beams.

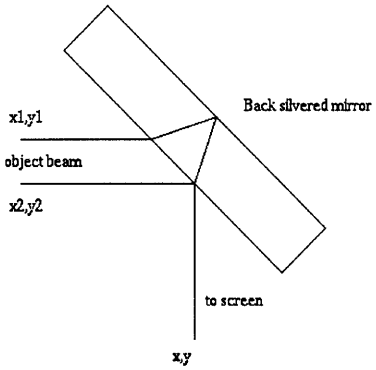

Figure 8: Interference of Two Beams

$$\Delta\rho(x,y) = \frac{\lambda N(x,y)}{Cl} \qquad \text{Eq. 3.3}$$

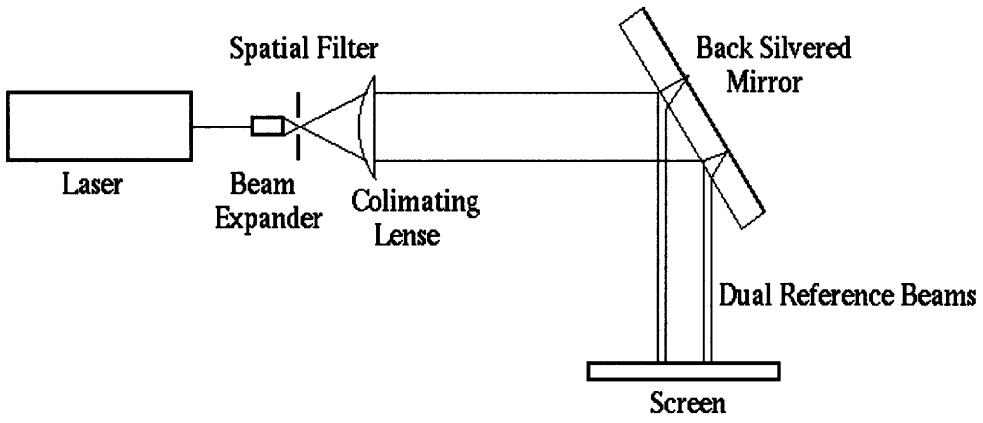

Figure 9: Shearing Interferometer Schematic

The shearing interferometer utilized at MIT included a 5 mW Helium Neon laser; a microscopic objective of numerical aperture 0.25; a spatial filter; a plano-convex lens of diameter 100 mm, focal length 150 mm; and a 150 mm square, 3mm thick back-silvered mirror. The components were arranged as depicted in the schematic shown in Figure 9. Due to triggering difficulties, no images were obtained during transient testing, though testing using a steady-state CO_2 jet with similar gradients in refraction index indicates that this technique could be applied to shock tunnel tests.

Shearography shows promise as a technique for quantifying the density field in shock tunnel-induced jet flows. Evaluating this method in view of the goals of the HSCT program, however, reveals difficulties. The 2-D assumption made by shearography can be overcome through the making of many simultaneous measurements from different radial positions around a jet, but this is not feasible for mixer-ejector testing due to limitations in optical access. Furthermore, like the Schlieren system, this method is focused on identifying changes in refractive index rather than quantifying mixing directly. Like the focused-Schlieren, shearography would have limited success in the MIT shock tunnel due to the weak density gradients associated with some test configurations. Shearography, while a possible technique for use in conjunction with shock tunnel nozzle testing in certain applications, is not a feasible technique for accomplishing the mixing measurement goals of the HSCT program.

3.4.3 Mie-Scattering System

The theoretical basis for mixing measurements made utilizing Mie-scattering has been explained previously in this thesis. The theory was applied in the MIT shock tunnel at two different times with two different experimental setups. Both attempts follow the schematic shown in Figure 10, but with different specific components.

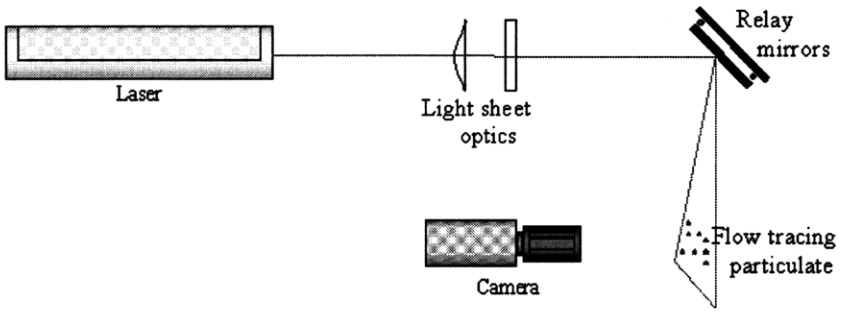

Figure 10: Mie-Scattering System Schematic

Vibration of the optical system was a concern because of the violence with which the shock tunnel fires. The instantaneous addition of mass to the room and the associated fluid movement generate mechanical oscillations as well as the acoustic ones which the facility is equipped to measure. To minimize the effects of any such vibration, the Uni-Strut framework was made a structurally rigid as possible and was insulated from floor vibration through rubber pads. The optics were all mounted to the same rigid structure so that any vibration experienced would be experienced by the entire system in the same way. The framework and optics were also kept at the maximum possible distance from the shock tunnel line of fire.

3.4.3.1 Seeding Technique

The seed selected for these tests was 0.4 micron diameter styrene particles suspended in water. As mentioned earlier, seed with a diameter on the order of 0.2 microns is required to faithfully follow flow through a trans-sonic shock. The 0.4 micron seed was found adequate to follow the flows experienced in the MIT shock tunnel. Seeding was accomplished in two stages to ensure sufficient seed density. First, the driven section was seeded while still at atmospheric pressure until seed had begun to leak from the nozzle at a sufficient density. Compressed air was bled through a TSI six-jet seeder and into the driven section. This was accomplished through a

tap in the wall of the driven section as far as possible from the nozzle end of the section. Once sufficient seed density had been obtained in this way, preparations for the shock tunnel test were begun, to include pumping the driven section to sub-atmospheric pressure and pumping the driver section to the correct pressure (~2-5 atm). The driven section was pumped down to 10% below its final value to allow the secondary seeding to occur. The secondary seeding was begun immediately before the tunnel was ready to fire, and more seed was added as air leaked through the seeder and into the shock tunnel to bring the driven pressure up to its prescribed value. In this way, the seed densities necessary for testing were consistently achieved.

3.4.3.2 Copper-Vapor Laser and Drum Camera Experimental Setup

The first attempt at mixing measurements using Mie-scattering involved a 15 W, 30 kHz pulsed copper-vapor laser illuminating the flow, with images recorded by a conventional 35 mm camera and a high-speed 40 kHz drum camera. No useful images were obtained using this method, so the details of the diagnostic will be relegated to Appendix A while the lessons learned are discussed here.

3.4.3.3 Importance of Trigger System in Copper-Vapor Laser System

Due to the extremely short duration of useful test time during a shock tunnel run, the trigger which synchronizes image capture with shock tunnel firing is of primary importance. The trigger used in this instance was an electrical circuit, which was broken when the plug from the end of the shock tunnel reached a certain distance from the nozzle exit. This trigger proved to be unsatisfactory due to the failure of the plug to accelerate fast enough. Figure 11 shows images taken with a high speed camera at 250 Hz. The image on the left shows the displacement of the plug used during the copper-vapor tests. As may be seen from the elapsed time (ET) counter in

the lower right-hand corner of the image, the plug has moved only 2-3 diameters downstream in the first 20 ms after shock tunnel firing. Based upon the design of the trigger used for the imaging system, this means that the copper-vapor laser/drum camera would not have begun recording images until after the useful test time of the shock tunnel. This triggering problem prevented any useful images from being obtained during the first experimental attempt. The plug-displacement problem was solved by the use of a much smaller and lighter plug of 1/8th" thick plastic which accelerates away from the nozzle sufficiently quickly to be well out of the imaging area before the useful test time has elapsed, as shown in the image on the right side. Furthermore, a reliable and accurate triggering system based upon the shock passage past the pressure transducers in the driven section of the shock tunnel was developed for subsequent tests.

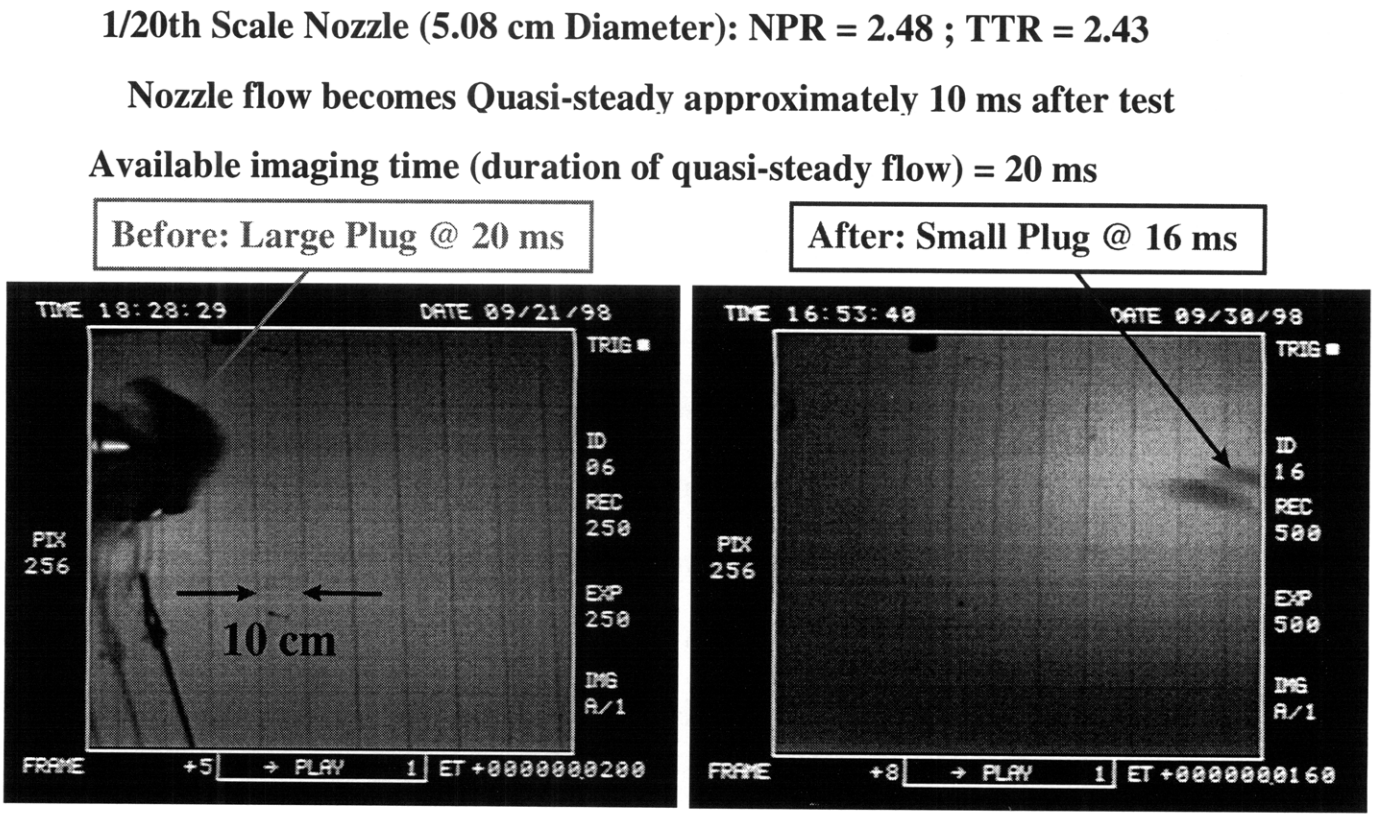

Figure 11: Plug Displacement

3.4.3.4 Argon-Ion Laser and Digital Imaging Equipment

A continuous-wave, 10 W all-lines Argon-Ion laser was used to illuminate the flow in the second experimental effort. The laser and associated optics were arranged in the same way as for the copper-vapor laser attempt. The image was captured by a 30 Hz, digital, 8-bit camera coupled to a shuttered and gated image intensifier. The image intensifier utilized a 60 mm 1:2.8 Nikon lens to focus upon the light sheet. A theoretical gain of 100,000 is possible with this image intensifier, but the practical gain limit is on the order of 1,000. Based upon a single electronic trigger, the image intensifier may be programmed for up to 63 independent exposures, each with a minimum duration of 20 ns and a minimum separation of 10 ns. The digital camera used was a 1,000 x 1,000 triggerable, progressive scan digital camera operating at 30 Hz. This operating requirement limited the images that the image intensifier could be programmed to acquire, as only one frame could be acquired by the digital camera during the test time, with one exception. The digital camera, while generally operating at 30 Hz, has the ability to take a single, separate exposure of ¼ millisecond duration immediately following the trigger, followed by the standard, 30millisecond frame. Thus after a single trigger, a pair of images may be obtained. The utility of this feature is limited, however, because the gain on the image intensifier may not be adjusted in the microsecond or less between the frames.

The image intensifier and camera were mounted at 90 degrees to the light sheet, at standoff distances ranging from 2 inches to 32 inches for nozzle sizes from ¼ inch to 4 inches, respectively. A beam-stop was added to prevent the light sheet from causing extraneous reflections. To minimize background illumination, a matte-black screen was placed behind the light sheet in the field of view. Furthermore, the light-sheet was trimmed to prevent reflections off the nozzle being tested.

The triggering system, shown by the first round of tests to be of vital importance, was based upon the passage of the incident shock wave through the test section of the shock tunnel. As the shock wave passed, pressure transducers detected a rapid pressure rise, which initiated a TTL trigger to the imaging system. This trigger worked flawlessly for the duration of the second experimental effort.

3.4.3.5 Results of Mie-Scattering Experiments

Four sets of images were obtained using the argon-ion laser set-up: ¼" nozzle at steady state, ¼" nozzle transient test, 0-1 diameters downstream for 4" nozzle transient test, and 1-3 bdiameters downstream for 4" nozzle transient test. In each case, an instantaneous image of 30 microseconds exposure and a time-average image of 5 milliseconds exposure were obtained.

The ¼" nozzle, steady-state images were obtained by pressurizing the entire shock tunnel to approximately 3 atmospheres using compressed air and maintaining that pressure. The jet may be seen exiting the nozzle in Figures 12 and 13. Maximum intensity is achieved several diameters downstream after the flow has expanded. This counter-intuitive result is explained by the fact that the intensity is not the result of illuminating the styrene seed, but is rather reflection from water vapor. The compressed air used to maintain the steady-state jet is not heated, so this jet has a TTR of 1. As the jet expands and reaches atmospheric pressure, the temperature within the jet drops along with the pressure according to the ideal gas law, causing condensation within the jet.

In Figures 14 and 15, the transient ¼" nozzle tests support this conclusion, as the maximum intensity is realized within the jet before the expansion and mixing process occurs. The nozzle is being supplied in this case by test gas at NPR~2.35, TTR~2.35. It is believed that

the higher temperature ratio prevents condensation within the jet. The reader will note the presence of background debris in this image, which will be discussed in section 3.5.1.

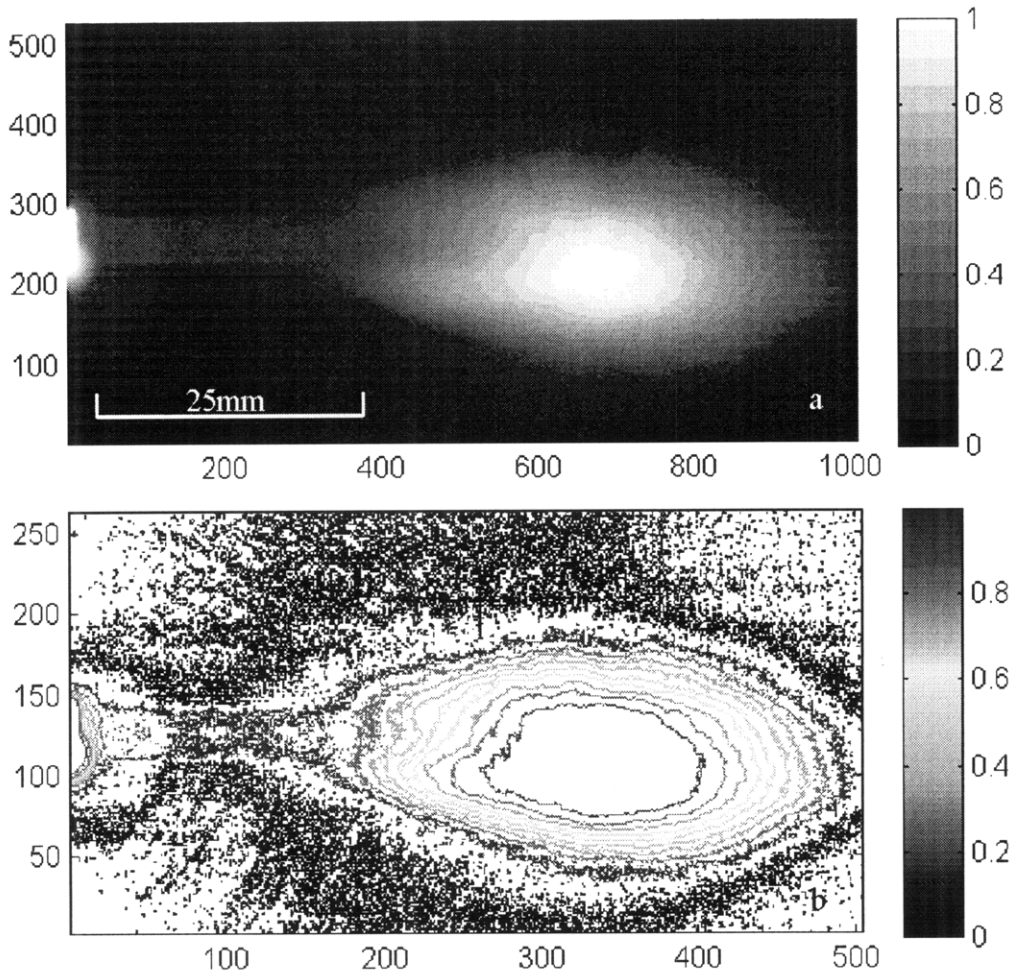

Figure 12: 1/4 inch nozzle, 5 millisecond exposure during steady-state testing, normalized greyscale and contour plots respectively

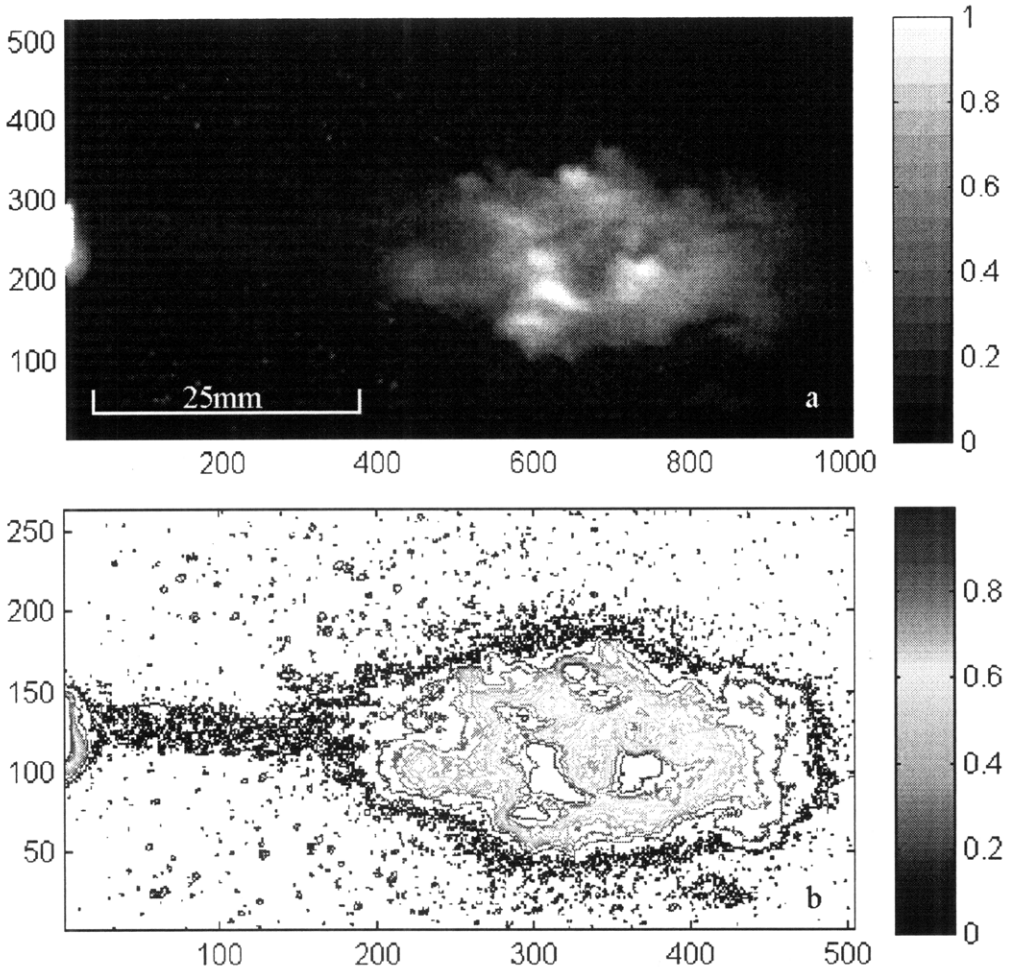

Figure 13: 1/4 inch conic nozzle, 30 microsecond exposure during steady-state test, normalized greyscale and contour plots respectively

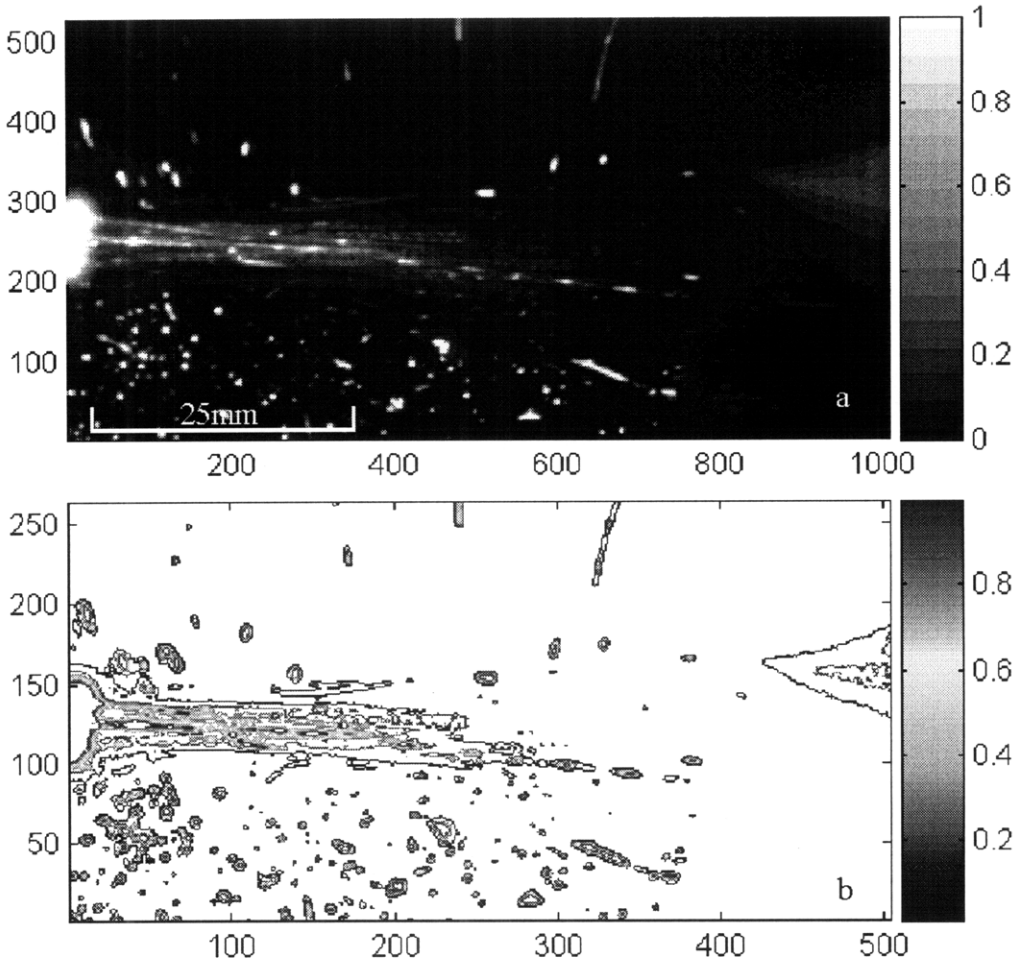

Figure 14: 1/4 inch conic nozzle, 5 millisecond exposure during transient test, normalized greyscale and countour plots respectively

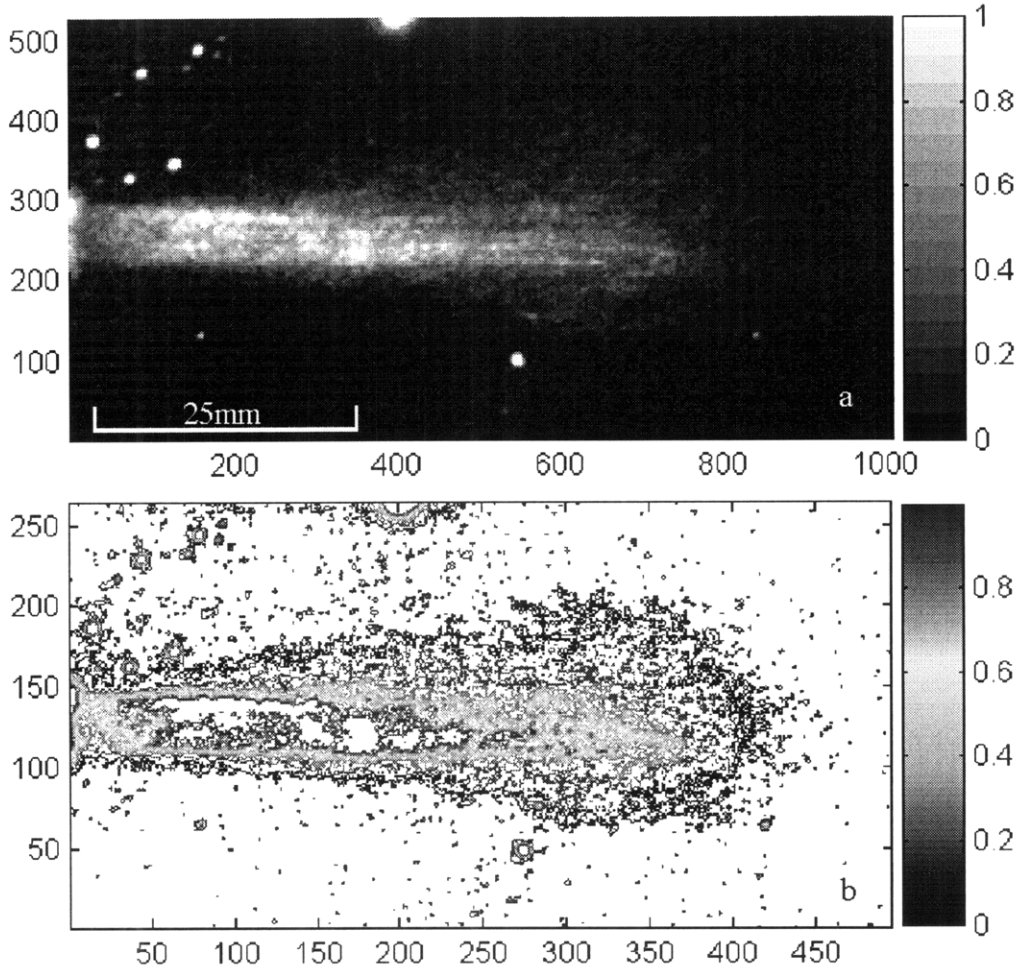

Figure 15: 1/4 inch conic nozzle, 30 microsecond exposure during transient test, normalized greyscale and contour plots respectively

While it is a useful diagnostic tool, the ¼" nozzle is far from the model scales desired for HSCT testing. The 4" nozzle is more representative of mixer-ejector nozzle models to be tested in terms of scale and exit area.

The 5 millisecond time-average exposure in Figure 16 shows the jet profile exiting the nozzle. The instantaneous exposure, Figure 17, illustrates the signal-to-noise ratio problem caused by insufficient laser power/intensifier gain for such a short exposure. The laser light profile for these tests was a Gaussian one due to the optics used, therefore the light intensity was greatest in the center of the sheet and faded toward the edges. These trends may be seen more clearly in Figures 18 and 19, images of the jet from 1-3 diameters downstream, and are addressed in the proposed system.

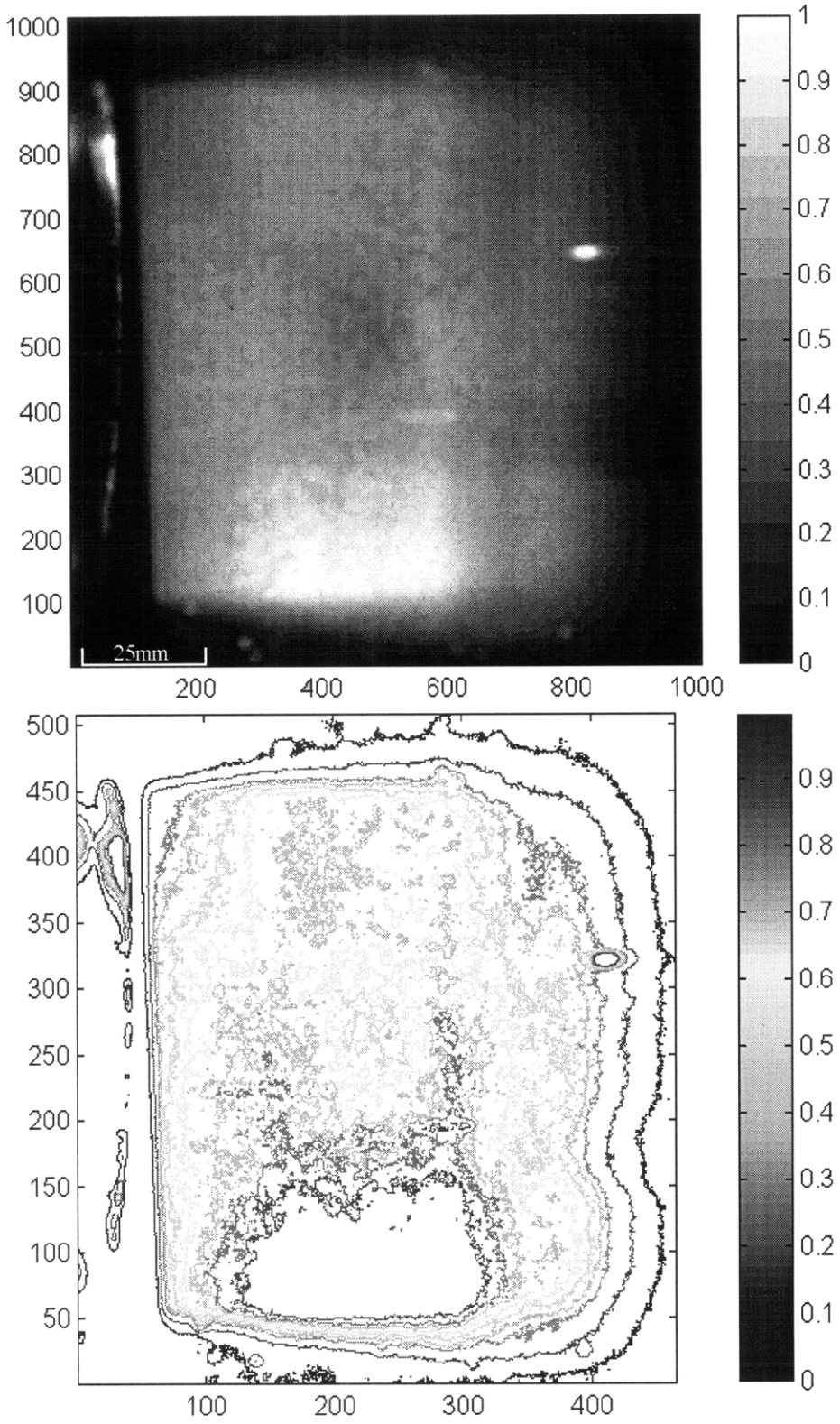

Figure 16: 4 inch conic nozzle, 0-1 Diameters downstream, 5 millisecond exposure, normalized greyscale and contour plots respectively

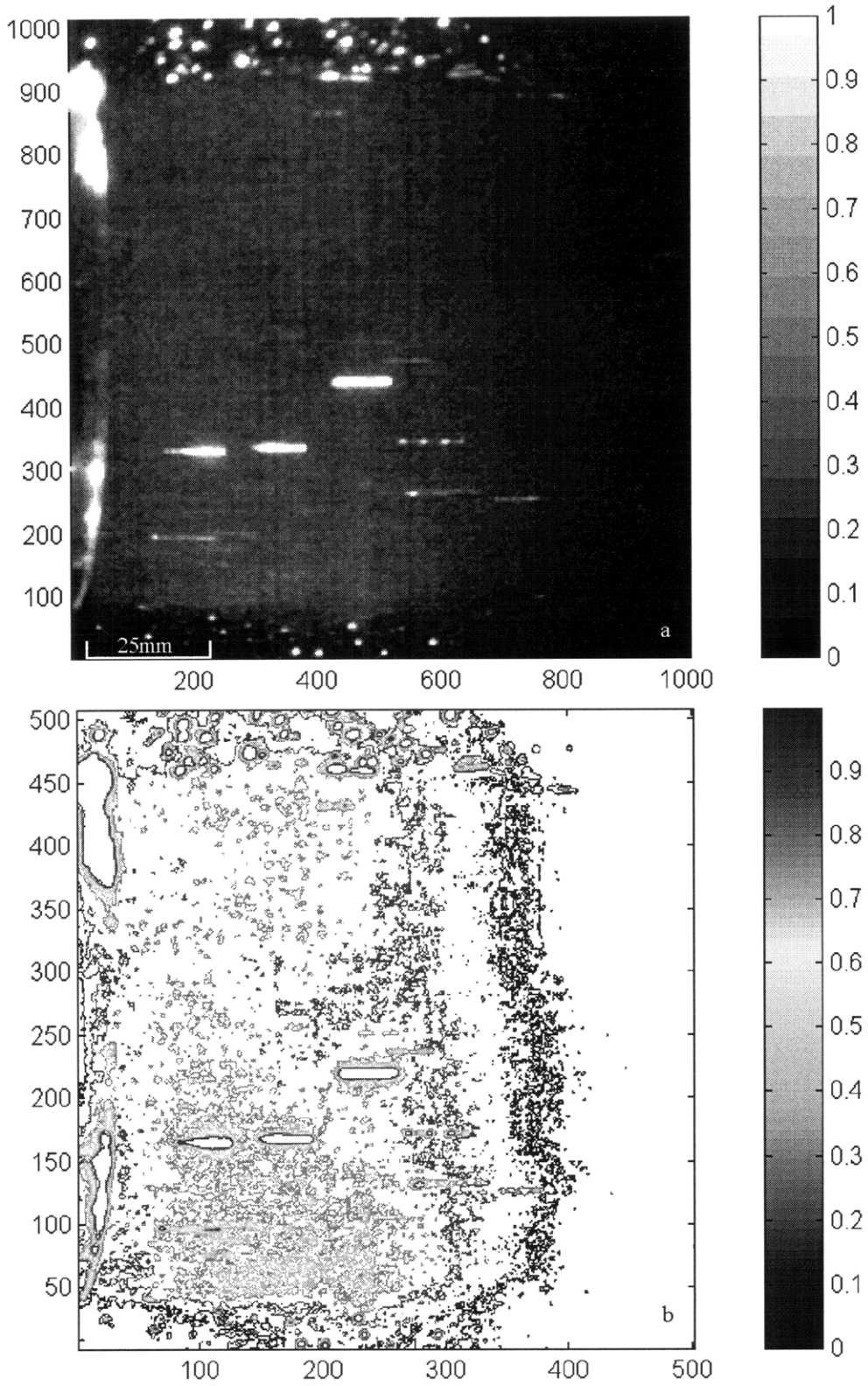

Figure 17: 4 inch conic nozzle, 0-1 Diameters downstream, 30 microseconds exposure, normalized greyscale and contour plots respectively

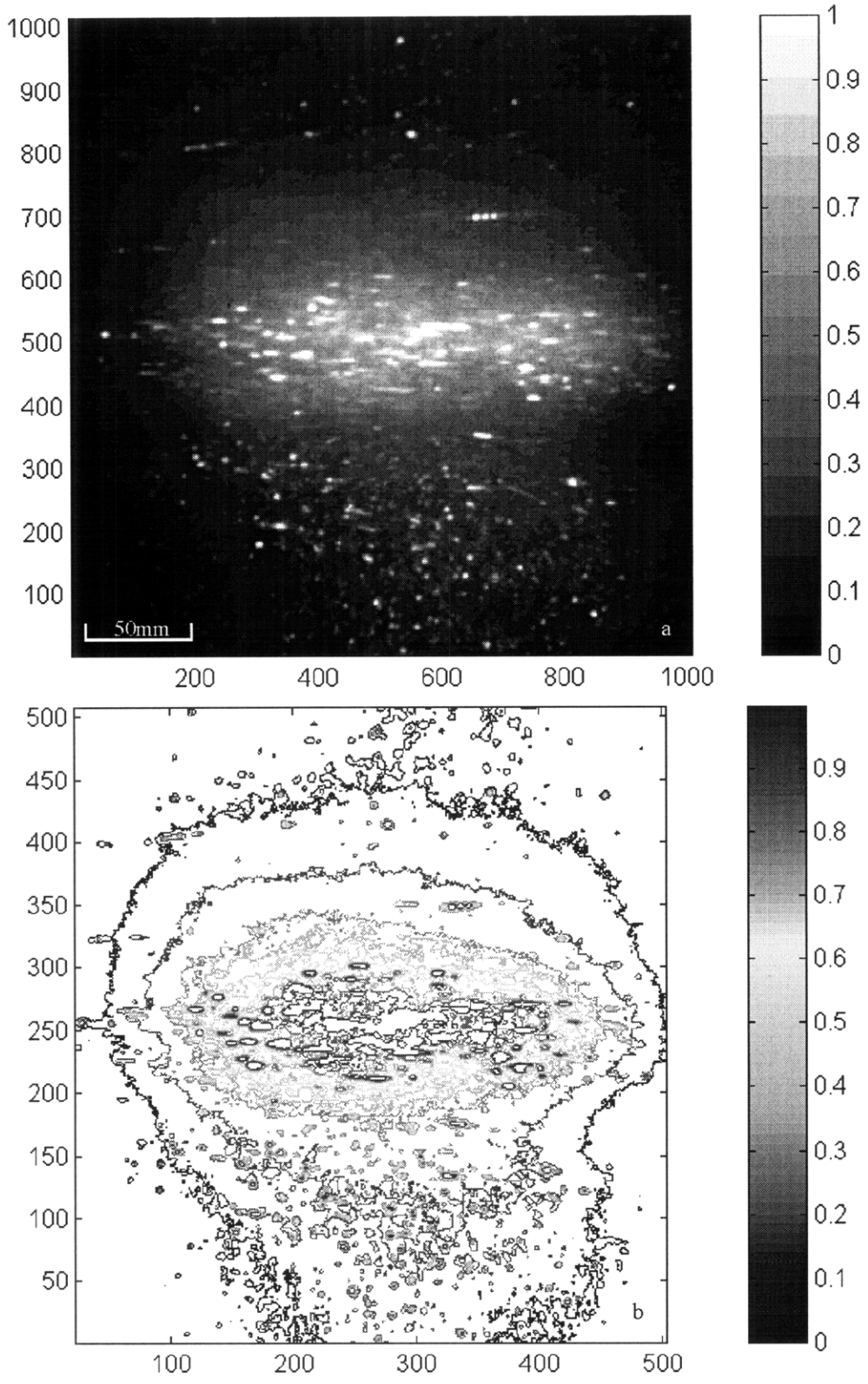

Figure 18: 4 inch conic nozzle, 1-3 Diameters downstream, 5 ms time-average exposure, Normalized greyscale and contour plots respectively

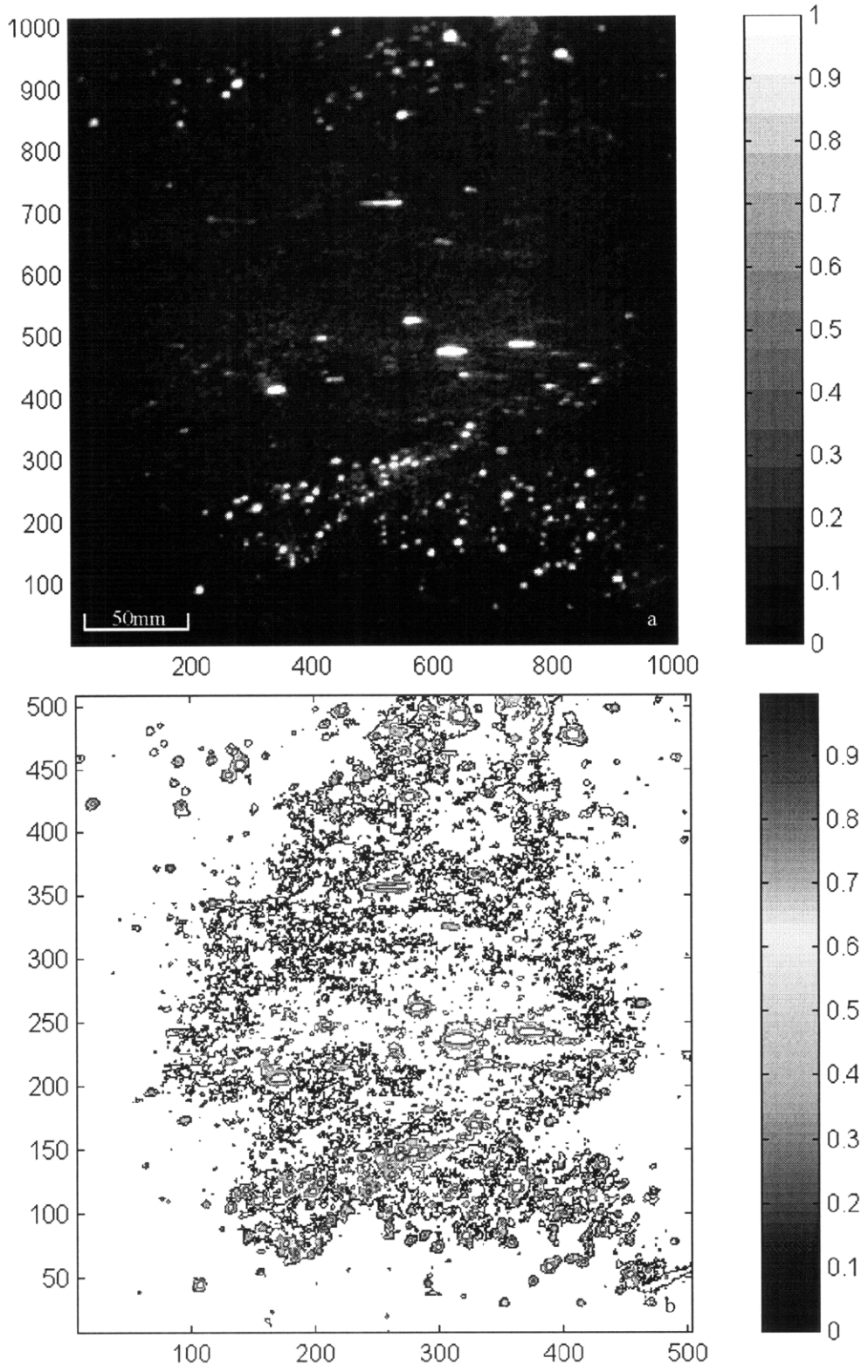

Figure 19: 4 inch conic nozzle, 30 microsecond exposure, 1-3 diameters downstream

3.4.4 Conclusions

In the course of evaluating the feasibility of mixing measurement using the MIT shock tunnel, three types of systems were considered: focused Schlieren, shearing interferometry, and Mie-scattering visualization. The latter is best-suited to the objectives of mixing measurements in the shock tunnel facility. The potential of the Mie-scattering method is shown by the results of the Mie-scattering tests that have already been done, but this potential has not yet been fully realized.

3.5 Proposed Mixing measurement system

This section proposes an experimental setup that will implement the Mie-scattering concept in the MIT shock tunnel environment to obtain quantitative mixedness data. The failings of previous attempts will be discussed, as will the features of the proposed system that rectify those failings. A detailed hardware list and experimental setup is also provided. Finally, an estimate of the expected typical uncertainty is presented.

3.5.1 Comparison to Previous System

While the previous measurements made using Mie-scattering provided some information as to the flow characteristics, there are some flaws in those measurements that can be corrected in the proposed system. First, since the mixing measurement is made on the basis of the light intensity reflected from particles in the flow, it is imperative that the light directed into the flow field be of uniform density. Failure to provide a uniform light sheet will lead to false density measurements: in a flow field with constant density, an area where the impinging light is of greater intensity will appear brighter and hence of higher density than an area where the light is less intense. The initial attempt at Mie-scattering measurements used cylindrical lenses which

shaped the light sheet into a Gaussian profile which was most intense in the center and faded toward the edges. This effect is especially obvious in Figure 16. This failing is corrected in the proposed system through the use of structured-light optics which have been developed for machine vision applications and are designed to provide a uniform intensity light sheet.

Another means by which the intensity measured can be corrupted is by unwanted velocity effects. If the exposure time of an image is of sufficient length, each seed particle will appear as a streak across several pixels of the image. Since the Mie-scattering method determines mixedness based on the number of illuminated pixels in a region and the intensity of these pixels, this velocity effect can introduce some uncertainty. To remove the velocity effect, the exposure or the illumination time must be such that the particles will be effectively frozen within one pixel. To accomplish this goal for the flows of interest to the HSCT program the exposure/illumination time must be on the order of a microsecond. The proposed system utilizes a pulsed laser to deliver 1-5 millijoule pulses with durations on the order of tens of nanoseconds. This insures that the proposed system will be capture images where local illumination intensity may be correlated directly to local primary flow density.

A third difficulty discovered during the most recent round of testing is interference from particles in the ambient air. The shock tunnel is designed to be used for acoustic measurements as well as for mixing and thrust measurements. To that end, the walls, ceiling, and floor of the shock tunnel are covered with approximately four inches of bulk fiberglass insulation. A layer of fiberglass cloth is placed over the insulation to keep most of the fiberglass in place, but the presence of fiberglass particles in the ambient air can not be eliminated, only alleviated, in the present form of the facility. The fiberglass in the test chamber atmosphere translates to background debris in the Mie-scattering images. This is true in spite of measures taken to

minimize the effect of such debris, such as a beam stop that absorbs laser radiation not passing through the imaging area and a matte black screen placed behind the jet. A further reduction in background debris is essential to making valid mixing measurements.

There are several possible means for accomplishing this. The first is to install an air filtration system to continually clean particulates from the test chamber atmosphere. This involves a major facility modification and also suffers from the handicap of fighting an enemy that will always exist, since the fiberglass insulation is needed for acoustic measurements. A second option is to replace the fiberglass absorber with one that will produce fewer particulates. This too is a major facility modification and could only be implemented at great cost to both time and money. The third, most promising alternative is to overpower the effect of background debris through the use of laser-induced fluorescence. Styrene dyed with fluoroscene and the 'FluoSpheres' of the medical world are two examples of seed particles which fluoresce when illuminated by laser light of the correct wavelength. Using such seed particles in the shock tunnel test gas would allow images to capture the far brighter seed particles without interference from background debris. This solution satisfies the need to eliminate background debris without the penalty of intrusive and expensive facility modifications.

3.5.2 Proposed System

The proposed system for mixing measurements is very similar to the one used in this feasibility study, with modifications only where necessary to improve the performance shortfalls identified above. A 10 Watt pulsed laser with a repetition rate on the order of 10 kHz and a pulse duration of 1 microsecond or less would provide the illumination for the images. The laser radiation would be shaped into a uniform light sheet through the use of a structured light optic and would pass through the flow of interest to be terminated in a beam stop. The light will

illuminate fluorescent seed particles of diameter equal to what was used before, but which are dyed to fluoresce when excited by the laser light. The reflected and emitted light is intensified using a image intensifier as before, and is captured by a triggerable, shuttered, progressive scan CCD camera operating at 30 Hz. This system adds the improvements discussed in the previous section to the fundamentally sound system concept that has already been proven. The proposed system follows the schematic of Figure 10. A detailed equipment list is shown to more fully specify the proposed system.

Equipment List
10 Watt, 10kHz pulsed Nd:Yag or copper vapor laser
Structured optics
Uni-strut frame and relay mirrors
Standard styrene or fluorescent 0.4 micron diameter seed
Multiple-jet seeder
Image intensifier
30 Hz triggerable, shuttered, progressive scan CCD camera
Optical filters and lenses

3.5.3 Estimate of feasibility and uncertainty for the proposed system.

A typical, un-intensified CCD camera requires about 10 mJ/cm^2 to capture a useful image. For a 10 ms time-averaged image with elastic scattering (normal, styrene seeding), that translates to 100 mW/cm^2. Using the proposed 10 W laser on a 100 cm^2 imaging area yields an illumination intensity of 100 mW/cm^2, which is the minimum required. Intensification is required to capture a larger imaging area or to improve the image intensity. An image-intensifier, such as the one used in the previous research effort, is capable of two orders-of-magnitude of intensification. The use of fluorescing seed would result in scattering intensities approximately one order of magnitude lower, due to the fact that only a specific wavelength is being captured. The filters which would select the wavelength of interest are not 100% inefficient. The order of magnitude decrease in scattered intensity is a cumulative estimate of the scattering and filtering

inefficiency and the loss of laser light emitted outside the selected wavelength. The intensification system is sufficient to enable imaging using the fluorescent seed.

For an instantaneous image, the exposure time must be short enough to capture each particle within one pixel. For the velocities of interest to the shock tunnel, this forces an exposure time on the order of one microsecond. A typical pulsed Nd:Yag laser is capable of delivering pulse intensities on the order of 400 mJ. A single pulse within the one-microsecond exposure time with elastic scattering throughout a 100 cm^2 imaging area would produce 4 mJ/cm^2 at the camera, which is sufficient for image capture. Again, fluorescent seeding would lead to inelastic scattering with an order-of-magnitude decrease in scattered light. The proposed intensification system would be necessary for the use of fluorescent seeding in the instantaneous case as well.

Depending upon the experimental setup, background illumination corrections, perspective corrections, or light sheet intensity variation corrections may be required.

Using the proposed system, it is estimated, from experience with similar systems and previously obtained results, that density may be determined throughout the seeded flow field to within 5% of the measured value with an optical resolution of 5-10 mm. The optical resolution is dependent upon the size of the imaged area.

4 Thrust Measurement System

4.1 System Background

4.1.1 Objective and Constraints

Thrust measurements must be made to a reasonable degree of accuracy using a limited number of supporting measurements. The goal for the system is measurement of thrust coefficient with an absolute uncertainty of better than 1%, recognizing that trends may then be resolved with an uncertainty less than or equal to the absolute uncertainty.

4.1.2 Design Rationale

Because the other forces acting upon the shock tunnel are at least equal to, and often an order of magnitude greater than the thrust force, measuring the force exerted by the entire shock tunnel on the backstop and then subtracting the endwall pressure forces would lead to higher than desired uncertainty. This is due to the higher ranges necessary for the force transducer at the backstop and the extremely high accuracy (0.01% FS) demanded of the pressure transducers on each end of the shock tunnel. Based on this preliminary analysis, a system was designed to measure the thrust produced by the nozzle utilizing force links at the interface between the nozzle and shock tunnel flanges was developed.

4.2 Theoretical Background

4.2.1 Conservation of Momentum

The integral form of the law of conservation of momentum in its most general form is:

$$\boxed{\sum F_x + F_o = \iiint_V \rho * \frac{d\vec{V}}{dt} * dV + \iint_S \rho * \vec{V} * (\vec{V} \bullet \hat{n}) dS} \qquad \text{(Eq 4.1)}$$

Thus the sum of all external forces and any force due to an accelerating reference frame is related to the time rate of change of momentum enclosed by a control volume plus the net momentum flux through the surface bounding that control volume.

From this most basic form, the F_o term may be dismissed for a non-accelerating frame of reference. In addition, the two cases to be considered below feature steady or quasi-steady flow, eliminating the unsteady momentum term. Thus the external forces, composed of pressure, viscous, body, and reaction forces, equal the net momentum flux out of the control volume.

$$\boxed{\sum F_x = \iint_S \rho * \vec{V} * (\vec{V} \bullet \hat{n}) dS} \qquad \text{(Eq 4.2)}$$

4.2.2 Off-Axis Nozzle

First consider a right-angle nozzle such as the one shown. Since incoming momentum flux is off-axis relative to the exit, the conservation of momentum equation simplifies to Equation 4.3.

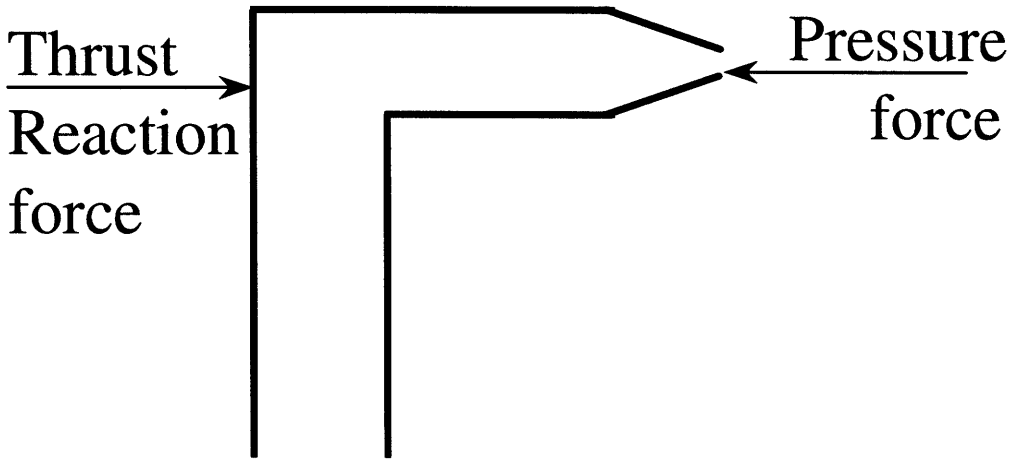

Figure 20: Off-Axis Nozzle Thrust Balance

$$Thrust - (P_e - P_o) * A_e = \dot{m}_e * U_e \qquad \text{(Eq 4.3)}$$

4.2.3 Straight-Line Nozzle

Alternatively, the control volume may be limited to the nozzle section of the shock tunnel. This is represented below with a magnification of the shock tunnel end and nozzle.

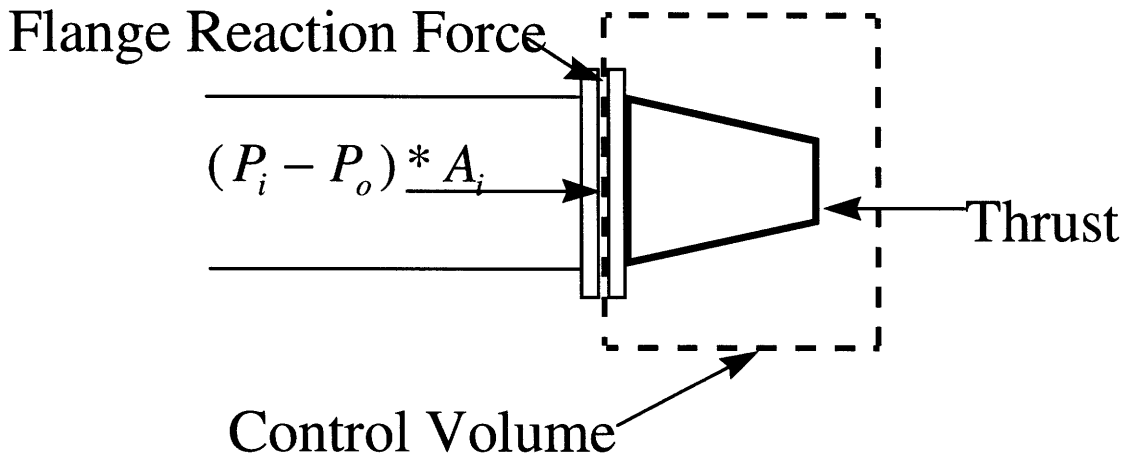

Figure 21: Shock tunnel Nozzle Force Balance

$$(P_i - P_o) * A_i - (P_e - P_o) * A_e + F_{reaction} = \dot{m}_e * U_e - \dot{m}_i * U_i \qquad \text{(Eq. 4.4)}$$

The same definition of thrust applies here as in the previous section. Substituting in the thrust relation of Equation 2 results in the equation governing the proposed thrust measurement system.

$$Thrust = F_{reaction} + \dot{m}_i * U_i + P_{i,gage} * A_i \qquad \text{(Eq 4.5)}$$

This formulation presents thrust as a function of the external (flange) reaction force, incoming momentum flux, and the pressure force at the control surface. It should be noted that these are all quantities which are constant for the duration of the shock tunnel test time.

4.3 Historical Background

Measurement of the thrust produced by flow through a nozzle is commonplace today. In steady-flow facilities, the measurement is most often accomplished by creating an experimental setup similar to the generic off-axis nozzle discussed in section 4.2.2. Using such a setup, steady-flow facilities typically measure thrust to within 0.25%.[21] The instrumentation used in steady-flow facilities is typically strain-gage based. The calculated resonant frequency for a typical strain-gage based load cell, as it would be applied in the MIT shock tunnel, is on the order of 400 Hz. The shock tunnel poses a unique thrust-measurement problem because of two basic differences from the steady-

[21] Fouladi, Kamran. Personal communication on the thrust measurement uncertainty attained at Boeing Nozzle Test Facility, NASA-Glenn Research Center CE22, and Fluidyne Corp. Pratt and Whitney. 6 May 1999.

state environment: an off-axis nozzle is not possible due to flow management concerns, and high dynamic response is needed.

Dynamic testing in conventional thrust-measurement facilities has demonstrated the need for a different approach in shock tunnel testing. Studies of a flight-type ejector at NASA Lewis Research Center Powered Lift Facility showed the difficulty of making transient measurements in steady-state facilities.[22] The test was intended to measure the dynamics associated with starting flow through an ejector intended for STOVL applications. To that end, it employed a burst-disk system to rapidly increase flow through the ejector. In an unchoked case, the nozzle pressure ratio was increased 36% over 150 milliseconds; in the second, choked condition the primary nozzle flowrate was increased about 17% over 100 milliseconds. For the unchoked condition, the thrust stand dynamics superimposed oscillations on the dynamic thrust data of the same order of magnitude as the thrust data. For the choked condition the amplitude of the oscillations was an order of magnitude less than the mean thrust value.

A stress-wave force balance has been developed at the University of Queensland for use in measuring multiple components of force experienced by scramjet components subjected to flows of one millisecond duration.[23] This balance mounts the test article at the end of 2 m sting of brass, which is suspended using fine wires. The thrust measurement is accomplished by measuring the stress waves which travel through the brass sting after flow begins to act upon the test article. The measured stress waves are then compared to stress waves observed earlier during calibration. While the accuracy

---

[22] Drummond, Colin K. "Preliminary Dynamic Tests of a Flight-Type Ejector." AIAA Paper 92-3261.
[23] Mee, D.J., W.J. Daniel, S.L. Tuttle, and J.M. Simmons. "Balances for the Measurement of Multiple Components of Force in Flows of a Millisecond Duration." AIAA Paper A96-12502.

of this system has not yet been quantified, the system has demonstrated the ability to measure the force line of action to within 1% and the axial/normal force ratio to within 5% of the numerically predicted values. While implementing an identical system in the MIT shock tunnel would not be feasible, this experimental effort indicates that measurement of highly dynamic thrust loads is possible.

4.4 Proposed System

4.4.1 System Overview

A schematic diagram of the proposed system is shown in Figure 22.

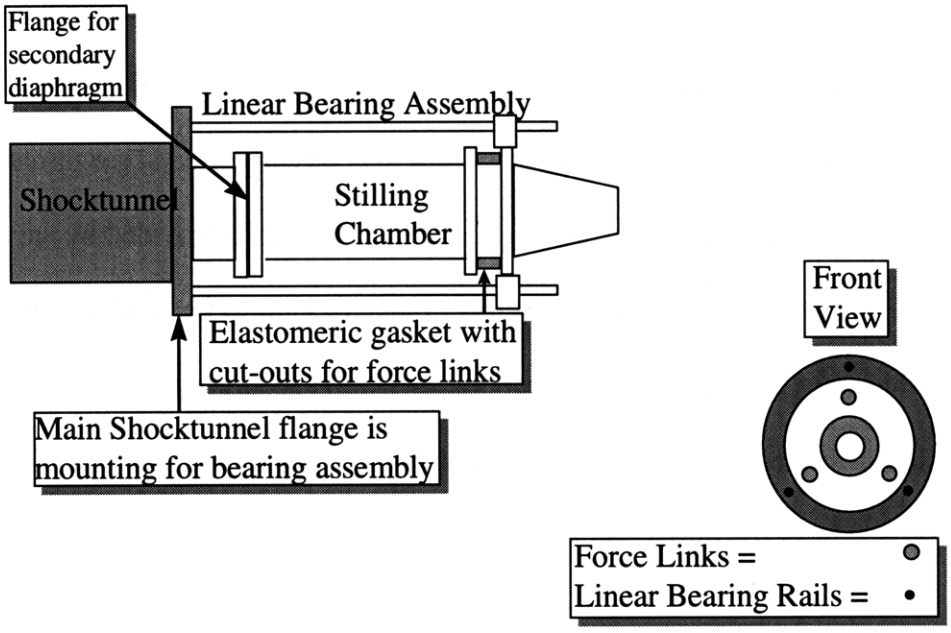

Figure 22: Thrust System Schematic

This thrust measurement system is designed to measure the force between the stilling chamber and the test article directly using three force links. An elastomeric gasket will cover the flange, with cut-out sections for the force links. The gasket will maintain the seal between the two flanges while carrying only a small fraction of the load. The linear bearing system is necessary to isolate the loading experienced by the force links to

the axial direction. The bearing system will support the weight of the model and prevent any shear forces or moments from being transmitted to the force links, while remaining nearly frictionless and hence transparent in the axial direction. The force being measured, which is denoted $F_{reaction}$ in the following force balance diagram, is related to the thrust produced by the nozzle through equation 4.1.

$F_{reaction}$ is measured directly by the three force links. A_{in} is only a function of the geometry of the stilling chamber, and will be determined by mechanical measurement. P_{in} is a static pressure measurement in the stilling chamber. This measurement will be made by 4 Kulite pressure transducers with high dynamic response. The four transducers will be arrayed circumferentially around the stilling chamber and then averaged to lower the uncertainty in the static pressure measurement. The momentum flux entering the metric section will be determined as follows. The mass flow will be calculated at the throat using knowledge of basic flow features and a knowledge of $C_{dp}*A_t$ provided by an independent calibration over the Reynolds number range of interest performed at a steady-state, cold-flow facility. Cold-flow calibration should accurately capture the throat area, as the short test times experienced with the shock tunnel prevent model heating and expansion. Mass flow at the throat will be calculated according to the Equation 4.6.

$$\dot{m} = C_{dp} * A_t * (\frac{\rho}{\rho_t} @ M = 1) * \rho_t * \sqrt{\gamma * R * (\frac{T}{T_t} @ M = 1) * T_{tp}} \qquad \text{Eq. 4.6}$$

The density and temperature ratio at choked conditions are well-known values. The shock tunnel is already equipped to accurately measure Nozzle Pressure Ratio (NPR) and Total Temperature Ratio (TTR), which provides the stagnation flow quantities needed. The

velocity entering the metric section will then be obtained from mass flow, density, and C_d*A_{in}, the latter of which will also be quantified through independent calibration in a cold flow calibration facility. This provides measurement of the average velocity entering the stilling chamber to within 1%.

4.4.2 Dynamic Modeling Analysis

A stiff load cell design is essential to satisfy the dynamic response requirements on the measurement of F_{act}, and is achieved by the choice of piezoelectric force links, which will experience a deflection of less than 100 micro-inches under a thrust load of 1,000 lb. In order to evaluate requirements for stiffness of the force links and to aid in the choice of an elastomer, the flange interface was modeled using the lumped-parameter system shown in Figure 23.

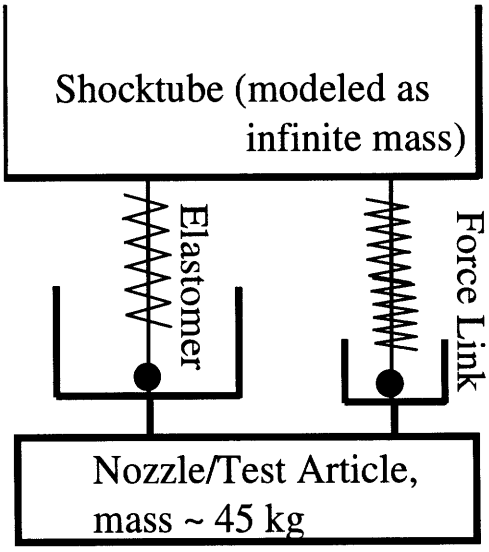

Figure 23: Dynamic Model of Balance

The goal of this thrust measurement system is to ensure that all of the thrust force is transmitted through the force links while maintaining sealing(elastomer), high dynamic

response of 1,000 Hz or better(high- stiffness force links), and behavior sufficiently far away from system resonance to assume that oscillations do not disrupt measurements. Ideally, the force link would be responsible for nearly all the stiffness in the system, while the elastomer would contribute all of the damping. In effect, the system can be modeled as a single spring and a single damper.

Linear roller bearings have been selected for this system. The coefficient of friction of the selected bearings is approximately 0.004. This translates to a frictional force that is on the order of 0.1% of a typical thrust load. Additionally, dynamic analysis performed on the design indicates that the stiffness of the force links will prevent the velocities and accelerations experienced by the bearings from being outside the capabilities of the roller bearings. The linear bearing system is therefore not modeled in the dynamic analysis.

The force link chosen for this system has a spring constant of 5,710,000 pounds per inch and a damping constant of 3,171 pounds. The elastomer of interest has a spring constant of 156,636 pounds per inch and a damping constant of 63,531 pounds. The relative magnitudes of these constants indicate that this design will closely approximate the ideal system described earlier. The stiffness of this thrust measurement system will yield a natural frequency of 1,300 Hz, which is sufficient for the thrust measurements of interest. Further modeling was performed for a thrust load of 500 pounds and spring and damping constants as indicated above to fully identify the vibrations the system may experience. Two different loading profiles were tested: a linearly increasing load and an exponentially increasing load.

Several different rise times were also tested to model the flow start-up period during which thrust attains its steady-state value. The 1-2 ms rise time approximates 1.5 flow-through times for the reference conic nozzles, while the 4 ms rise time does the same for the LSMS at the baseline (NPR=2.48, TTR=2.43) condition. The results of all the above-mentioned analysis may be found in Appendix A. The time response of the system to a load applied over 2 ms is shown in Figure 24.

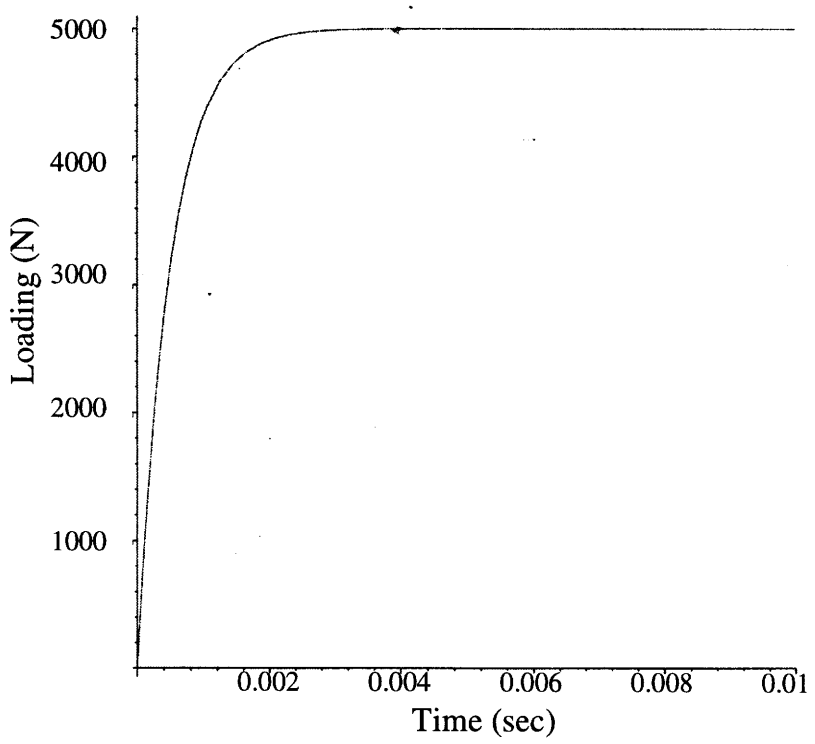

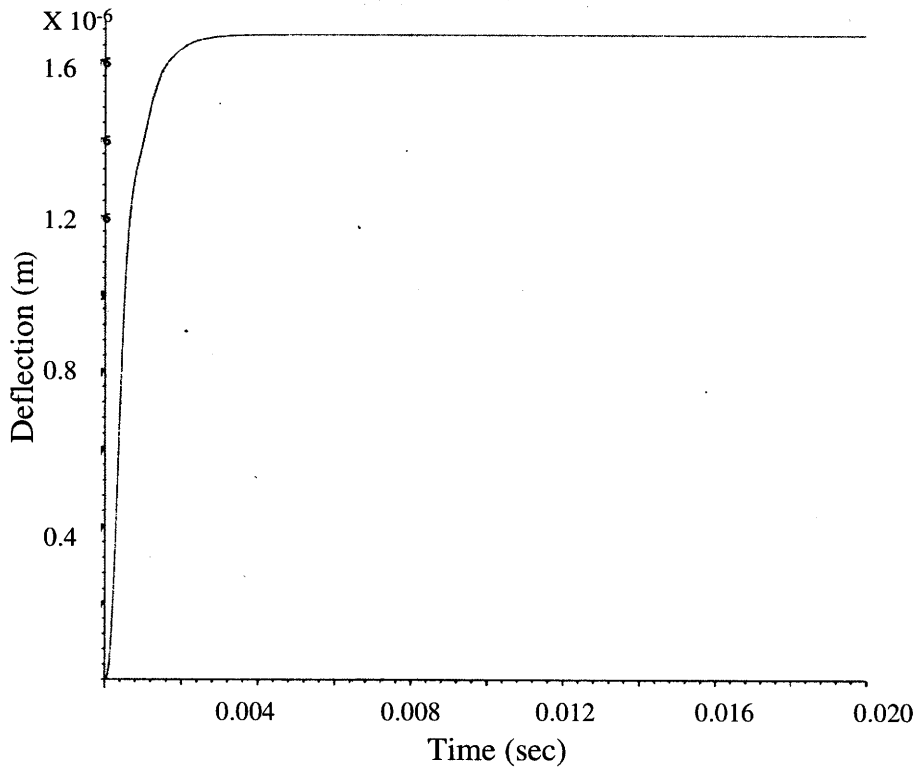

Figure 24: Dynamic Response of Proposed System

In summary, the dynamic modeling of the system showed that in all cases the vibrations of the system were negligible 5 ms after the quasi-steady thrust level was reached. For reference, acoustic data is not normally gathered from the first 10 ms of flow because of slight variations in the reservoir total pressure, which are damped out after the first 10 ms, followed by 10-20 ms of quasi-steady conditions, as shown in Figure 4. Thus thrust data taken from the quasi-steady condition would not be contaminated.

4.4.3 Uncertainty Analysis

An uncertainty analysis was performed using standard theory for uncertainty propagation according to the following equation.

$$\sigma_A = \sqrt{\left(\frac{\partial A}{\partial X} * \sigma_X\right)^2 + \ldots + \left(\frac{\partial A}{\partial Y} * \sigma_Y\right)^2}$$

where A is a function of (X,..., Y) Eq. 4.7

The specific equations for this thrust system may be found in Appendix B for reference . Table 1 lists the contributors to system uncertainty, their uncertainty in the baseline system configuration, and the source for that uncertainty estimate.

Variable	Baseline Value	Estimate Source
Ptp	690/2 Pa	Kulite product specifications, 0.1% FS error, 100 psi range
Pin	345/2 Pa	Kulite product specifications, 0.1% FS error, 50 psi range
P	69 Pa	Paroscientific reference transducer product specifications
T	0.1 K	Vaisala temperature and humidity sensor specifications
cinit	0.5 m/s	Adtek system data acquisition rate controlled
CdpAt	0.000041 m^2	Uncertainty in cold-flow calibration, as quoted by cal facility
CdAin	0.000131 m^2	Uncertainty in cold-flow calibration, as quoted by cal facility
Fact	0.4448 N	Piezoelectric force link specifications
Ain	0.000017 m^2	Estimated uncertainty in geometric measurement of spool piece

Table 1: Uncertainty Sources

The uncertainty goal for thrust measurements in the MIT shock tunnel is 1% of nozzle thrust coefficient, $C_{T,D} = \frac{F_{actual}}{F_{ideal,primary}}$. This method of uncertainty propagation analysis predicts an uncertainty in the nozzle thrust coefficient of 0.8% based on the baseline case of Nozzle Pressure Ratio(NPR)=2.48 and Total Temperature Ratio(TTR)=2.43. The uncertainty in thrust coefficient is predicted to be 1.1% for NPR=1.51, TTR=1.82, and 0.8% for NPR=3.43, TTR=2.91. Analysis indicates that the force measurement is not the primary source of uncertainty. On the contrary, uncertainties in effective nozzle throat

area, stilling chamber static pressure, and primary total pressure have contributions to the system uncertainty that are an order of magnitude greater than the expected uncertainty of the force measurement itself. Table 2 summarizes the sources of uncertainty and their relative importance. The values presented in Table 2 show the percent change in the baseline error value that occurs should that source of uncertainty be eliminated. For example, if the primary flow total pressure ($P_{t,p}$) could be measured with no uncertainty, the system uncertainty of 1.1 for the NPR = 1.51 condition would decrease by 8.9% to 1.0. The full uncertainty analysis is attached in Appendix B.

	Percent change in baseline error by variable			
Variable	NPR=1.51	NPR=2.48	NPR=3.43	NPR=4.0
Ptp	**8.9**	**2.7**	**1.3**	**0.8**
Pin	**11.2**	**3.4**	**1.5**	**1.0**
P	0.2	0.1	0.0	0.0
T	0.0	0.0	0.0	0.0
Cinit	0.0	0.0	0.0	0.0
CdpAt	**25.2**	**48.3**	**57.3**	**60.4**
CdAin	0.3	0.4	61.0	0.5
Fact	0.2	0.1	0.0	0.0
Ain	**8.5**	**7.1**	**6.0**	**5.5**
Baseline Error Values(%)	**1.1**	**0.9**	**0.8**	**0.8**

Table 2: Uncertainty Sensitivity Analysis

5 Conclusions

5.1 Mixing Diagnostic

The theoretical basis for a Mie-scattering mixing diagnostic has been presented. Past efforts at focused Schlieren, interferometry, and Mie-scattering diagnostics are presented. A Mie-scattering imaging system is presented which improves upon previous efforts and is expected to provide density measurements to within 5% with an optical resolution of 5-10 millimeters.

5.2 Thrust Diagnostic

Previous attempts at dynamic thrust measurements have shown problems with applying strain-gage technology to such an experiment. An understanding of the differences between steady-state and shock tunnel testing environments is used as the basis for the design of a thrust measurement system with high dynamic response. The proposed system is described in detail, and supporting dynamic modeling results are presented which indicate that the system will be able to accurately measure dynamic thrust loads. Uncertainty analysis is presented which predicts measurement of thrust coefficient to within approximately 1%.

5.3 Future Work

The work discussed in this thesis lays the theoretical and design foundations for mixing and thrust measurement systems of highly transient nozzle flows, specifically related to the MIT shock tunnel. Based upon this work, the implementation and validation of such systems is the next step towards the more cost-effective and timely

transient testing of jet engine exhaust nozzle designs. Prior to any such implementation effort, a review of the relevant instrumentation technologies should be undertaken, as these are advancing quickly, particularly in the area of imaging.

6 Appendix A: Detail of Copper-Vapour Laser Attempt at Mie-Scattering Mixing Measurements

The copper-vapor laser emitted light at two wavelengths, 510.6 and 578.2 nm. The pulse rate of the laser ranged from 9 to 30 kHz, giving pulse durations in the 10 to 40 ns range. The laser head and power supply were both placed in the shocktube control room, adjacent to the test cell into which the shocktube discharges. The laser beam was passed through a beam tube in the dividing wall and was then directed using a system of mirrors mounted to an Uni-Strut frame.

As mentioned earlier, a conventional 35 mm camera was used in this measurement scheme. Due to the need to maintain a stable operating temperature, the laser was required to be continuously emitting. This placed the burden for triggering and shuttering upon the camera, which posed a problem. The camera's mechanical shutter had an opening time of approximately 80 ms, which was simply not fast enough to capture a run time of only 20 ms. The 35 mm camera was not suitable for this test.

The high-speed drum camera proved to be more capable. 125 lines per mm of resolution were available at operating frequencies up to 40 kHz. The drum has a 1000 mm circumference, which allows 80 12.5 x 35 mm images to be obtained. The drum camera also has a mechanical shutter with an opening time in the millisecond range.

Appendix B: Detailed Thrust Measurement System Uncertainty Analysis

```
> restart;
> Ctd:=(Fact+mdot*Vin+Pin*Ain)/Fip;
```

$$Ctd := \frac{Fact + mdot\ Vin + Pin\ Ain}{Fip}$$

Since the force we measure directly is not thrust, the thrust coefficient arises from a combination of the measured thrust, incoming streamthrust and pressure forces acting on the control volume around the nozzle. The comphrehensive equation for the uncertainty in the thrust coefficient is shown below.

```
> Uncertainty_Ctd:=((diff(Ctd,Fact)*Uncertainty_Fact)^2+(diff(C
  td,Fip)*Uncertainty_Fip)^2+(diff(Ctd,mdot)*Uncertainty_mdot)^
  2+(diff(Ctd,Vin)*Uncertainty_Vin)^2+(diff(Ctd,Pin)*Uncertaint
  y_Pin)^2+(diff(Ctd,Ain)*Uncertainty_Ain)^2)^0.5;
```

$$Uncertainty\_Ctd := \left(\frac{Uncertainty\_Fact^2}{Fip^2} + \frac{(Fact + mdot\ Vin + Pin\ Ain)^2\ Uncertainty\_Fip^2}{Fip^4} + \frac{Vin^2\ Uncertainty\_mdot^2}{Fip^2} + \frac{mdot^2\ Uncertainty\_Vin^2}{Fip^2} + \frac{Ain^2\ Uncertainty\_Pin^2}{Fip^2} + \frac{Pin^2\ Uncertainty\_Ain^2}{Fip^2} \right)^{.5}$$

```
> R:=287;
```

$$R := 287$$

```
> g:=1.35;
```

$$g := 1.35$$

Find the Uncertainty in the ideal thrust term.

```
> Fip:=CdpAt*Ptp*(2*g^3/(g-1)*(2/(g+1))^((g+1)/(g-1))*(1-1/((Pt
  p/P)^((g-1)/g))))^0.5;
```

$$Fip := 1.414213562\ CdpAt\ Ptp \left(2.380559353 - 2.380559353 \frac{1}{\left(\frac{Ptp}{P} \right)^{.2592592593}} \right)^{.5}$$

```
> Uncertainty_Fip:=((diff(Fip,Ptp)*Uncertainty_Ptp)^2+(diff(Fip
  ,CdpAt)*Uncertainty_CdpAt)^2+(diff(Fip,P)*Uncertainty_P)^2)^0
  .5;
```

$$Uncertainty\_Fip := \left(\left(\right. \right.$$

$$1.414213562\ CdpAt\left(2.380559353 - 2.380559353\frac{1}{\left(\frac{Ptp}{P}\right)^{2592592593}}\right)^{.5}$$

$$+ .4364136159\frac{CdpAt\ Ptp}{\left(2.380559353 - 2.380559353\frac{1}{\left(\frac{Ptp}{P}\right)^{2592592593}}\right)^{.5}\left(\frac{Ptp}{P}\right)^{1.259259259}P}\Bigg)^{2}$$

$$Uncertainty\_Ptp^2 + 1.999999999$$

$$Ptp^2\left(2.380559353 - 2.380559353\frac{1}{\left(\frac{Ptp}{P}\right)^{2592592593}}\right)^{1.0}Uncertainty\_CdpAt^2$$

$$+ .1904568441\frac{CdpAt^2\ Ptp^4\ Uncertainty\_P^2}{\left(2.380559353 - 2.380559353\frac{1}{\left(\frac{Ptp}{P}\right)^{2592592593}}\right)^{1.0}\left(\frac{Ptp}{P}\right)^{2.518518518}P^4}\Bigg)^{.5}$$

Find the uncertainty in the velocity term.

```
> rhot:=Ptp/(R*Ttp);
```

$$rhot := \frac{1}{287}\frac{Ptp}{Ttp}$$

```
> mdot:=CdpAt*(0.6339*rhot)*(g*R*0.8333*Ttp)^0.5;
```

$$mdot := .03968691843\frac{CdpAt\ Ptp}{Ttp^{.5}}$$

```
> Vin:=mdot/(rhot*CdAin);
```

$$Vin := 11.39014559\frac{CdpAt\ Ttp^{.5}}{CdAin}$$

Put in the equations for uncertainty in Total Temperature

```
> TTR:=(2*(g-1)*Ms^2+(3-g))*((3*g-1)*Ms^2-2*(g-1))/((g+1)^2*Ms^
  2);
```

$$TTR := .1810774106\frac{(.70\ Ms^2 + 1.65)(3.05\ Ms^2 - .70)}{Ms^2}$$

```
> Ms:=cinit/(g*R*T)^0.5;
```

$$Ms := .05080332854\frac{cinit}{T^{.5}}$$

```
> Ttp:=TTR*T;
```

$$Ttp := 70.15844274 \frac{\left(.001806684734 \frac{cinit^2}{T^{1.0}} + 1.65\right)\left(.007871983483 \frac{cinit^2}{T^{1.0}} - .70\right)T^{2.0}}{cinit^2}$$

```
> Uncertainty_Vin:=((diff(Vin,Ptp)*Uncertainty_Ptp)^2+(diff(Vin
  ,T)*Uncertainty_T^2+(diff(Vin,CdAin)*Uncertainty_CdAin)^2+dif
  f(Vin,cinit)*Uncertainty_cinit)^2+(diff(Vin,P)*Uncertainty_P)
  ^2+(diff(Vin,CdpAt)*Uncertainty_CdpAt)^2)^0.5;
```

$$Uncertainty\_Vin := \left(\left(\left(47.70229238\ CdpAt\left(-.00002844438478 \frac{cinit^2}{T^{1.0}} - .01172409344 + 2.0 \frac{\left(.001806684734 \frac{cinit^2}{T^{1.0}} + 1.65\right)\left(.007871983483 \frac{cinit^2}{T^{1.0}} - .70\right)T^{1.0}}{cinit^2}\right)Uncertainty\_T^2 \Big/ \left(\frac{\left(.001806684734 \frac{cinit^2}{T^{1.0}} + 1.65\right)\left(.007871983483 \frac{cinit^2}{T^{1.0}} - .70\right)T^{2.0}}{cinit^2}\right)^{.5} CdAin\right) + 9102.034793\ CdpAt^2 \left(\frac{\left(.001806684734 \frac{cinit^2}{T^{1.0}} + 1.65\right)\left(.007871983483 \frac{cinit^2}{T^{1.0}} - .70\right)T^{2.0}}{cinit^2}\right)^{1.0} Uncertainty\_CdAin^2 \Big/ CdAin^4 + 47.70229238\ CdpAt\left(.003613369468 \frac{T^{1.0}\left(.007871983483 \frac{cinit^2}{T^{1.0}} - .70\right)}{cinit} + .01574396697 \frac{\left(.001806684734 \frac{cinit^2}{T^{1.0}} + 1.65\right)T^{1.0}}{cinit}\right)$$

$$-2\frac{\left(.001806684734\frac{cinit^2}{T^{1.0}}+1.65\right)\left(.007871983483\frac{cinit^2}{T^{1.0}}-.70\right)T^{2.0}}{cinit^3}\Bigg)$$

$$Uncertainty\_cinit \Big/ \Bigg($$

$$\left(\left(\frac{\left(.001806684734\frac{cinit^2}{T^{1.0}}+1.65\right)\left(.007871983483\frac{cinit^2}{T^{1.0}}-.70\right)T^{2.0}}{cinit^2}\right)^{.5} CdAin\right)^2 +$$

$$9102.034793\left(\frac{\left(.001806684734\frac{cinit^2}{T^{1.0}}+1.65\right)\left(.007871983483\frac{cinit^2}{T^{1.0}}-.70\right)T^{2.0}}{cinit^2}\right)^{1.0}$$

$$\left.Uncertainty\_CdpAt^2 \Big/ CdAin^2\right)^{.5}$$

```
> Uncertainty_mdot:=((diff(mdot,Ptp)*Uncertainty_Ptp)^2+(diff(m
  dot,T)*Uncertainty_T^2+(diff(mdot,CdAin)*Uncertainty_CdAin)^2
  +diff(mdot,cinit)*Uncertainty_cinit)^2+(diff(mdot,P)*Uncertai
  nty_P)^2+(diff(mdot,CdpAt)*Uncertainty_CdpAt)^2)^0.5;
```

$$Uncertainty\_mdot := \Bigg(.00002244992098$$

$$\frac{CdpAt^2\ Uncertainty\_Ptp^2}{\left(\frac{\left(.001806684734\frac{cinit^2}{T^{1.0}}+1.65\right)\left(.007871983483\frac{cinit^2}{T^{1.0}}-.70\right)T^{2.0}}{cinit^2}\right)^{1.0}} + \Bigg(-$$

$$.002369067379\ CdpAt\ Ptp\left(-.00002844438478\frac{cinit^2}{T^{1.0}}-.01172409344+2.0\frac{\left(.001806684734\frac{cinit^2}{T^{1.0}}+1.65\right)\left(.007871983483\frac{cinit^2}{T^{1.0}}-.70\right)T^{1.0}}{cinit^2}\right)Uncertainty\_T^2$$

$$\Big/\left(\frac{\left(\left(.001806684734\frac{cinit^2}{T^{1.0}}+1.65\right)\left(.007871983483\frac{cinit^2}{T^{1.0}}-.70\right)T^{2.0}\right)^{1.5}}{cinit^2}\right)-$$

$$.002369067379\ CdpAt\ Ptp\left(.003613369468\frac{T^{1.0}\left(.007871983483\frac{cinit^2}{T^{1.0}}-.70\right)}{cinit}+.01574396697\frac{\left(.001806684734\frac{cinit^2}{T^{1.0}}+1.65\right)T^{1.0}}{cinit}-2\frac{\left(.001806684734\frac{cinit^2}{T^{1.0}}+1.65\right)\left(.007871983483\frac{cinit^2}{T^{1.0}}-.70\right)T^{2.0}}{cinit^3}\right)$$

$$Uncertainty\_cinit\Big/\left(\left(\frac{\left(.001806684734\frac{cinit^2}{T^{1.0}}+1.65\right)\left(.007871983483\frac{cinit^2}{T^{1.0}}-.70\right)T^{2.0}}{cinit^2}\right)^{1.5}\right)^2+$$

$$.00002244992098\left(\frac{Ptp^2\ Uncertainty\_CdpAt^2}{\left(\left(\frac{\left(.001806684734\frac{cinit^2}{T^{1.0}}+1.65\right)\left(.007871983483\frac{cinit^2}{T^{1.0}}-.70\right)T^{2.0}}{cinit^2}\right)^{1.0}\right)^5}\right)$$

```
> Uncertainty_Ttp:=((diff(Ttp,cinit)*Uncertainty_cinit)^2+(diff
```

```
(Ttp,T)*Uncertainty_T)^2)^0.5;
```

$$Uncertainty\_Ttp := \left(\left(\left(.2535083749 \frac{T^{1.0}\left(.007871983483 \frac{cinit^2}{T^{1.0}} - .70 \right)}{cinit} + 1.104572205 \frac{\left(.001806684734 \frac{cinit^2}{T^{1.0}} + 1.65 \right) T^{1.0}}{cinit} - 140.3168855 \frac{\left(.001806684734 \frac{cinit^2}{T^{1.0}} + 1.65 \right)\left(.007871983483 \frac{cinit^2}{T^{1.0}} - .70 \right) T^{2.0}}{cinit^3} \right)^2 Uncertainty\_cinit^2 + \left(-.001995613741 \frac{cinit^2}{T^{1.0}} - .8225441383 + 140.3168855 \frac{\left(.001806684734 \frac{cinit^2}{T^{1.0}} + 1.65 \right)\left(.007871983483 \frac{cinit^2}{T^{1.0}} - .70 \right) T^{1.0}}{cinit^2} \right)^2 \right)^5 Uncertainty\_T^2 \right)$$

All of the above equations work out for specific NPR and TTR cases as follows. This assumes that both the shocktube and stilling chamber pressures are measured with 4 transducers, that the stilling chamber uses transducers with a range of 50 psi and an uncertainty of 0.1% FS.

```
> Uncertainty_Ptp:=690/2;
```

$$Uncertainty\_Ptp := 345$$

```
> Uncertainty_Pin:=345/2;
```

$$Uncertainty\_Pin := \frac{345}{2}$$

```
> Uncertainty_P:=69;
```

$$Uncertainty\_P := 69$$

```
> Uncertainty_T:=0.1;
```

$$Uncertainty\_T := .1$$

```
> Uncertainty_cinit:=0.5;
```

$$Uncertainty\_cinit := .5$$

Uncertainty in CdpAt is set to 0.75% of estimated CdpAt, in accordance with discussion with

Bill Johanson

```
> Uncertainty_CdpAt:=0.000041187;
```

$$Uncertainty\_CdpAt := .000041187$$

```
> Uncertainty_CdAin:=0.000131;
```

$$Uncertainty\_CdAin := .000131$$

```
> Uncertainty_Ain:=0.0000174774;
```

$$Uncertainty\_Ain := .0000174774$$

```
> Uncertainty_Fact:=0.4448;
```

$$Uncertainty\_Fact := .4448$$

Atmospheric Conditions and Constants

```
> P:=101325;
```

$$P := 101325$$

```
> T:=293;
```

$$T := 293$$

```
> CdpAt:=0.0054916;
```

$$CdpAt := .0054916$$

```
> CdAin:=0.0174774;
```

$$CdAin := .0174774$$

```
> Ain:=0.0174774;
```

$$Ain := .0174774$$

For the NPR=1.51 Condition:

```
> Ptp:=153000;
> Pin:=151000;
> cinit:=561;
> mdot;
> TTR;
> Fact:=0.95*Fip-mdot*Vin-Pin*Ain;
> Uncertainty_Vin;
> Uncertainty_mdot;
> Uncertainty_Ttp;
> Uncertainty_Fip;
```

$$Ptp := 153000$$

$$Pin := 151000$$

$$cinit := 561$$

$$1.444447406$$

$$1.818881157$$

$$Fact := -2204.003699$$

$$.7544991150$$

$$.01134215156$$

.6029236568

5.231590188

```
> Uncertainty_Ctd;
```

.01123855702

For the NPR=2.48 Condition

```
> Ptp:=251286;
> Pin:=249000;
> cinit:=698;
> mdot;
> TTR;
> Fact:=0.95*Fip-mdot*Vin-Pin*Ain;
> Uncertainty_Ctd;
```

$Ptp := 251286$

$Pin := 249000$

$cinit := 698$

2.051217637

2.432977159

$Fact := -3237.632596$

.008513784680

For the NPR= 3.43 Condition

```
> Ptp:=347544;
> Pin:=342000;
> cinit:=790;
> mdot;
> TTR;
> Fact:=0.95*Fip-mdot*Vin-Pin*Ain;
> Uncertainty_Ctd;
```

$Ptp := 347544$

$Pin := 342000$

$cinit := 790$

2.594095325

2.909863770

$Fact := -4179.236284$

.008018542078

For the NPR=4.0 Condition

```
> Ptp:=405300;
> Pin:=395019;
> cinit:=900;
> mdot;
> TTR;
```

```
> Fact:=0.95*Fip-mdot*Vin-Pin*Ain;
> Uncertainty_Ctd;
```

$$Ptp := 405300$$

$$Pin := 395019$$

$$cinit := 900$$

$$2.738246215$$

$$3.551674398$$

$$Fact := -4684.950192$$

$$.007884833459$$

```
> Ctd;
>
>
```

$$.9500000000$$